J. Fluid Mech. (2006), *vol.* 568, *pp.* 19–54.
doi:10.1017/S0022112006001686 Printed in the United Kingdom

Dynamics of a stratified shear layer with horizontal shear

By S. BASAK AND S. SARKAR

Department of Mechanical and Aerospace Engineering, University of California San Diego, 9500 Gilman Drive, La Jolla, CA 92093-0411, USA

(Received 30 August 2005 and in revised form 22 March 2006)

The evolution of a stratified shear layer with mean shear in the horizontal direction, orthogonal to gravity, is numerically investigated with focus on the structural organization of the vorticity and density fields. Although the Reynolds number of the flow increases with time, facilitating instabilities and turbulence, the bulk Richardson number signifying the level of stratification also increases. Remarkably rich dynamics is found: turbulence; the emergence of coherent core/braid regions from turbulence; formation of a lattice of dislocated vortex cores connected by thin horizontal sheets of collapsed density and vorticity; density-driven intrusions at the edges of the shear layer; and internal wave generation and propagation. Stratification introduces significant vertical variability although it inhibits the vertical velocity. The molecular dissipation of turbulent kinetic energy and of turbulent potential energy are both found to be substantial even in the case with highest stratification, and primarily concentrated in thin horizontal sheets. The simulation data are used to help explain how buoyancy induces the emergence of columnar vortex cores from turbulence and then dislocates these cores to eventually form a lattice of 'pancake' eddies connected by thin sheets with large vertical shear (horizontal vorticity) and density gradient.

1. Introduction

Stratified horizontal shear flows involving small-scale turbulence occur in a variety of situations: in oceanic and atmospheric flows around topography, at the edges of energetic ocean currents, in coastal fronts, in river outflows, and behind self-propelled bodies. The prototypical case of the evolution of a stratified shear layer where the velocity varies in the horizontal direction, orthogonal to gravity, has not been previously considered and is the subject of the current investigation.

The simplest case of stratified horizontal shear flow, an unbounded flow with constant mean shear perpendicular to a linear mean density gradient, was numerically simulated by Jacobitz & Sarkar (1998, 1999). Turbulence was found to be more energetic and with larger vertical buoyancy flux when a given level of mean shear was horizontal rather than vertical. This observation was attributed to two reasons: first, stratification does not directly affect the Reynolds shear stress and production of turbulent kinetic energy in horizontal shear flow and, second, turbulence remains three-dimensional so that the enhanced turbulent kinetic energy results in augmented vertical transport. It was also found that, at a critical value of the Richardson number, turbulence decays in both cases, but this critical value is larger in horizontal shear flow than vertical shear flow. Horizontal shear flow near a wall was investigated by Armenio & Sarkar (2004) who simulated channel flow past sidewalls. They found

an increase in turbulence levels and eddy diffusivity with respect to those observed in previous studies of channel flow with vertical shear (Komori *et al.* 1983; Garg *et al.* 2000; Armenio & Sarkar 2002). Turbulent wakes behind spheres and other bluff bodies have both horizontal and vertical shear. The growth of the wake in the vertical direction is quickly arrested with subsequent collapse, while it continues to grow horizontally. The mean velocity profile in the cross-stream direction is inviscidly unstable leading to the formation of long-lived eddies with large horizontal extent and small vertical extent in the far wake as observed in the laboratory experiments of Lin & Pao (1979), Spedding, Browand & Fincham (1996), Spedding (1997), Bonnier, Bonneton & Eiff (1998), the DNS of Gourlay *et al.* (2001), and the large-eddy simulations (LES) of Dommermuth *et al.* (2002). Also, three-dimensional, small-scale turbulence is found to be inhibited. Internal gravity waves were observed in the wake experiment of Bonneton, Chomaz & Hopfinger (1993) and also in the simulations of Gourlay *et al.* (2001) and Diamessis, Domaradzki & Hesthaven (2005). The stabilization of an initially turbulent jet by stratification has been experimentally studied by Voropayev, Smirnov & Brandt (2001) who find that the jet breaks down into a collection of vortex dipoles.

Shear layers with horizontal shear have been observed in the ocean. Flament *et al.* (2001) have studied a zonal horizontal shear flow off the island of Hawaii using drifting buoys and sea-surface height anomaly and find that the initially thin shear layer grows by vortex pairing. Munk *et al.* (2000) show visualizations of sea spiral eddies obtained using sunglint, and analyse the dynamics of the spiral eddies. A nice example of Kelvin–Helmholtz (KH) rollers in a horizontal shear layer is provided by their figure 2. Horizontal shear instabilities at the Norwegian Coastal Current front were observed using synthetic aperture radar by Johannessen *et al.* (1996). The scale of the horizontal shear in the preceding examples is of the order of 1–100 km and rotational effects are important. Farmer *et al.* (1995), combining acoustic imaging with CTD surveys, observed strong horizontal shears, 0.02–0.10 s^{-1}, on a scale of 100 m in a tidal convergence front in the Haro Strait. It is difficult to quantitatively observe horizontal shear at scales less than tens of metres although there have been a handful of efforts as discussed by Müller *et al.* (1986). Although the present work, where rotational effects are neglected, does not directly bear on the mesoscale horizontal shear flows that have typically been the subject of field studies, the work is relevant to smaller, submesoscale shear layers during their growth from very small size. The dynamics of such shear layers and their contribution to horizontal and vertical transport is of fundamental interest.

The problem of a shear layer that grows horizontally between two parallel, vertically infinite fluid streams with a relative horizontal velocity, see figure 1, in a stratified medium with constant buoyancy frequency, N, is investigated here using direct numerical simulation (DNS). The flow instabilities associated with the shear layer velocity profile (summarized later) are different from those in the wake or the jet. A notable difference is that the shear layer has KH rollers having the same sign of vorticity, unlike the opposite-signed vortices in a wake and in a jet. Both uniform shear flow and channel flow are not susceptible to inviscid instabilities of the inflectional mean profile studied here. As will be seen later, there are qualitative differences in the effect of stratification shown here with respect to other flows with horizontal shear studied previously: uniform shear, channel flow, wake and jet.

The evolution of a unstratified shear layer under a variety of conditions is summarized below to provide a basis for comparison. A laminar shear layer is subject to the following sequence of events: the fundamental KH instability develops

into rollers and braids, the subharmonic pairing instability leads to pairings of these rollers, and three-dimensional secondary instabilities tend to form streamwise vorticity. Winant & Browand (1974) identified KH rollers and their pairing in a low-*Re* laboratory shear layer. KH rollers develop spanwise variability (Browand & Troutt 1980; Comte, Lesieur & Lamballais 1992) and spanwise non-uniform pairing can occur (Chandrsuda *et al.* 1978; Collis *et al.* 1994; Comte *et al.* 1992). Brown & Roshko (1974) found rollers, braids and pairing of rollers in their planar visualizations of high-*Re* shear layers. The studies of Hernan & Jimenez (1982), Dimotakis & Brown (1976), and Hussain (1983) show that tearing, partial pairing and amalgamation are also important at high *Re* while Bell & Mehta (1990) do not observe distinct core/braid structures at high *Re*. Rogers & Moser (1994) simulated a shear layer, that starts from a turbulent boundary layer, up to a self-similar stage and, furthermore, found that spanwise-coherent rollers were not distinct in this stage. It is thought that at high *Re*, there is eventually a 'mixing transition', that is, development of strong three-dimensionality from initially quasi-two-dimensional dynamics. An instability of the elliptical vortex core, Pierrehumbert & Widnall (1982), and an instability of the hyperbolic braid region, Klaassen & Peltier (1991), have been identified theoretically as instabilities that could trigger this mixing transition. Three-dimensional instabilities of the shear layer have been studied experimentally by Hussain (1983), Bernal & Roshko (1986), Lasheras & Choi (1988), Nygaard & Glezer (1991) among others, and numerically by Corcos & Lin (1984), Metcalfe *et al.* (1987), Moser & Rogers (1993), among others.

Unlike horizontal shear layers, the effect of stratification on vertical shear layers has been widely studied (Thorpe 1973; Koop & Browand 1979; Fernando 2003; Strang & Fernando 2001; Smyth & Moum 2000*a*, *b*; Staquet 2000; Caulfield & Peltier 2000; Lee & Caulfield 2001). Here, stratification opposes the overturning motion of the primary KH billows. Caulfield & Peltier (2000) studied the linear and nonlinear evolution of small disturbances and found the route to turbulence, the so-called 'mixing transition', is substantially affected by buoyancy. The bulk Richardson number, Ri_b, grows in the vertical shear layer and stratification eventually dominates so that, eventually, the shear layer cannot grow further in the vertical (cross-stream) direction and turbulence collapses.

A general feature of strongly stratified flows with horizontal Froude number $Fr_h = u_h/Nl_h \ll 1$ is that *layers* of quasi-horizontal eddying motion called pancake eddies occur as found in decaying turbulence in the laboratory (Fincham, Maxworthy & Spedding 1996; Praud, Fincham & Sommeria 2005), in DNS studies of initially isotropic turbulence (Metais & Herring 1989; Herring & Metais 1989; Kimura & Herring 1996), and in the wake (Spedding 2002). The 'pancakes' are significantly larger laterally than vertically and separated by thin zones with large vertical shear. Numerical simulations of a model problem with flow initiated by Taylor–Green vortices with $Fr_h = O(1)$ by Riley & deBruynKops (2003) showed that, although the horizontal scale of the vortices increased with time, the characteristic vertical length decreased, and the vertical shear between the vortical structures intensified to maintain the gradient Richardson numbe, $Ri_g < 1$, leading to small-scale instabilities and overturning. A scaling analysis by these authors shows that the likelihood of small-scale instabilities and turbulence increases with the Reynolds number, *Re*. The analysis of Lilly (1983) had suggested the formation of vertically decoupled layers of motion with strong interspersed vertical shear. Majda & Grote (1997), analysing the flow equations in the limit of high stratification, found that initial columns of vertical vorticity, when perturbed by a small vertical shear, evolve

towards a set of truncated pancake-like structures. The linear instability analysis of Billant & Chomaz (2000*b*) indicates a buoyancy-related instability, the zigzag instability, that helps explain the slicing of a stratified counter-rotating vortex pair that was observed experimentally by Billant & Chomaz (2000*a*). The vertical scale, l_v, of the zigzag instability is such that $Fr_v = u_h/Nl_v \rightarrow O(1)$, instead of tending to zero.

A localized region of stratified turbulence is known to form *intrusions* at its boundary with the surrounding quiescent fluid. These intrusions, driven by horizontal gradients of density, consist of locally mixed fluid from the turbulent zone that propagate outward into the stratified external region with the outflow being balanced by the influx of fresh unmixed fluid toward the mixed layer. Intrusions at the boundary of a vertically extensive region of stratified turbulence, created by oscillating grids or rakes, have been investigated by Thorpe (1982), Ivey & Corcos (1982), Browand, Guyomar & Yoon (1987), and Liu, Maxworthy & Spedding (1987). De-Silva & Fernando (1998) show that the collapse of a single turbulent patch has similar features. Intrusions by turbulence have also been observed in natural water bodies (Caldwell, Brubaker & Neal 1978). In the present problem too, a vertically extensive region of turbulence, forced by shear between the two horizontally flowing streams, interacts with the surrounding stratified ambient. The potential formation of intrusions and the effect of mean shear on the propagation of these intrusions is of interest.

A stratified fluid can support internal gravity waves of frequency less than the buoyancy frequency N excited by vortical fluctuations. Internal waves are radiated by grid-generated turbulence during its deepening in a stratified fluid (Linden 1975; E & Hopfinger 1986; Dohan & Sutherland 2003), by coherent structures in the stratified far wake (Lin *et al.* 1992; Bonneton *et al.* 1993; Gourlay *et al.* 2001), by KH rollers in a vertical shear layer (Sutherland, Caulfield & Peltier 1994; Sutherland & Linden 1998), and by density-driven intrusive gravity currents (Flynn & Sutherland (2004) and references therein). In all the above flows, there is a region of turbulence and/or coherent vortices in a vertically limited region that emits internal gravity waves that travel into the adjacent stratified ambient, above or below the flow. In the present problem, the region of flow is vertically infinite, but nevertheless there is the possibility of turbulence and internal waves coexisting within the shear layer, as well as waves that propagate away sideways into the surrounding stratified ambient.

The overall objective of the paper is to investigate stratification effects in a horizontal-shear layer, a flow in which instabilities are continuously generated by the inflectional mean velocity profile, the Reynolds number keeps increasing so that nonlinearity remains important, but at the same time the horizontal Froude number (Richardson number) keeps decreasing (increasing) so that stratification is also important. The sequence of events characterizing transition from infinitesimal perturbations to turbulence, and the effect of stratification on a shear layer which already has broadband, finite-amplitude perturbations are both of interest. Only the second problem is investigated here with the following objectives. First, the structural organization of the vorticity field will be examined, comparisons to the unstratified case will be made, and the coupling between buoyancy and vorticity will be identified. Second, the vertical structure of the velocity and buoyancy fields will be examined for layering, a mechanism by which horizontal eddying motions have localized sites of strong dissipation and vertical mass transport. This mechanism could be operative in environmental horizontal shear layers. Third, the simulations will be examined for intrusions and internal wave emission which are modes of interaction of the shear layer with its ambient, made possible because of stratification.

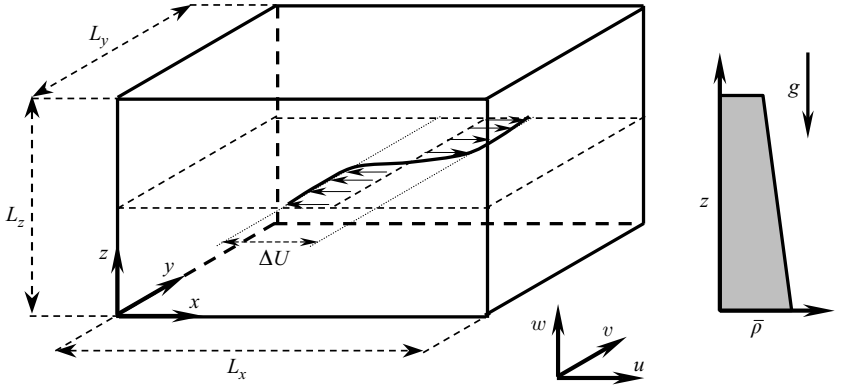

FIGURE 1. Schematic of a temporally evolving horizontal shear flow with vertical stratification.

The paper is organized as follows. Section 2 describes the problem formulation. Section 3 discusses the evolution of the mean flow. The evolution of the vorticity and the density fields are described in § 4 and § 5, respectively. Section 6 describes the locations of large dissipation and mixing in this flow and discusses the overall mixing energetics. The work is summarized in § 7.

2. Formulation

A schematic of the model problem studied is shown in figure 1. A shear layer, subject to an imposed vertical stratification $\mathrm{d}\overline{\rho}/\mathrm{d}z$, develops between two streams with equal and opposite velocity. The velocity difference between the streams is ΔU. The cross-stream thickness of the shear layer, measured by the vorticity thickness $\delta_\omega = \Delta U(\mathrm{d}\overline{u}/\mathrm{d}y)_{max}$, increases with increasing time. The computational domain consists of a rectangular box with lengths L_x, L_y and L_z in the x (streamwise), y (cross-stream) and z (vertical, spanwise) directions, respectively. x, y, z and x_1, x_2, x_3 are used interchangeably for the axes.

The non-dimensionalized, conservative form of the Navier–Stokes equations with the Boussinesq approximation,

$$\frac{\partial u_k}{\partial x_k} = 0, \tag{2.1}$$

$$\frac{\partial u_i}{\partial t} + \frac{\partial (u_k u_i)}{\partial x_k} = -\frac{\partial p}{\partial x_i} + \frac{1}{Re_0}\frac{\partial}{\partial x_k}\frac{\partial u_i}{\partial x_k} - Ri_{b,0}\rho'\delta_{i3}, \tag{2.2}$$

$$\frac{\partial \rho}{\partial t} + \frac{\partial (u_k \rho)}{\partial x_k} = \frac{1}{Re_0 Pr}\frac{\partial}{\partial x_k}\frac{\partial \rho}{\partial x_k}. \tag{2.3}$$

are solved numerically. Velocity, length and time are non-dimensionalized with reference values ΔU, $\delta_{\omega,0}$ (the initial value of δ_ω) and $\delta_{\omega,0}/\Delta U$, respectively. The density fluctuation ρ' in momentum conservation (2.2), is non-dimensionalized using $\Delta\rho = (\mathrm{d}\overline{\rho}/\mathrm{d}z)\delta_{\omega,0}$. Here, $\delta_{\omega,0}$, has been used as the vertical length scale for convenience; it will be seen later that buoyancy determines the vertical length scale when the stratification is strong. The pressure deviation, p, with respect to the mean hydrostatic pressure is non-dimensionalized by $\rho_0(\Delta U)^2$. The quantities Re_0 and $Ri_{b,0}$ are the

initial values of Reynolds number,

$$Re = \frac{\Delta U \delta_\omega}{\nu}, \tag{2.4}$$

and bulk Richardson number,

$$Ri_b = -\frac{g}{\rho_o}\frac{\mathrm{d}\overline{\rho}}{\mathrm{d}z}\frac{\delta_\omega^2}{\Delta U^2} = \frac{N^2\delta_\omega^2}{\Delta U^2}. \tag{2.5}$$

Ri_b is defined using horizontal shear and vertical stratification, an analogue to that in vertically sheared and stratified flow, and can be interpreted as a ratio of the buoyancy forcing to the shear forcing, or as the (squared) ratio of two time scales imposed on the fluctuations.

The total density ρ, consisting of a linearly varying mean part $\overline{\rho}(z)$ (see figure 1) and a fluctuating part $\rho'(x, y, z, t)$, can be written as

$$\rho = \overline{\rho}(z) + \rho'(x, y, z, t)\,. \tag{2.6}$$

The value of stratification, $\mathrm{d}\overline{\rho}/\mathrm{d}z$, is chosen to prescribe the initial Ri_b, and initially $\rho'(x, y, z, t) = 0$.

The mean velocity field is initialized as follows:

$$\overline{u}_1(y) = \frac{\Delta U}{2}\tanh\left(-\frac{y}{2\delta_{\theta,0}}\right),\ \overline{u}_2 = 0,\ \overline{u}_3 = 0, \tag{2.7}$$

where $\delta_{\theta,0}$ is the initial value of momentum thickness defined by

$$\delta_\theta = \int_{y_{min}}^{y_{max}} \left(\frac{1}{4} - \left(\frac{\overline{u}_1(y)}{\Delta u}\right)^2\right)\mathrm{d}y. \tag{2.8}$$

Here y_{min} and y_{max} denote the extent of the computational domain in the y-direction. Note that $\delta_{\theta,0} = \delta_{\omega,0}/4$. Broadband fluctuations are used to accelerate transition to turbulence with the following spectrum:

$$E(k) = (k/k_0)^4 \exp(-2(k/k_0)^2). \tag{2.9}$$

The energy spectrum peaks at k_0, corresponding to the wavelength $1.684\delta_{\omega,0}$, which is significantly smaller than the most amplified KH mode, $7.23\delta_{\omega,0}$. The initial turbulence energy, $q^2 = \overline{u_i' u_i'} = 0.0288\Delta U^2$, is large enough to achieve quick transition to turbulence, and also has an exponential decay from the centreline to the edges of the initial shear layer. Different initial conditions are discussed in the Appendix to show that the late-time statistical evolution and dynamics are not significantly changed. Periodic boundary conditions are used in the streamwise x-direction and vertical z-direction for the velocity and pressure fields and the fluctuating part of the density field, ρ'. The cross-stream y-direction boundary conditions are: $p' = 0$, $\rho' = 0$, and $\partial u_i/\partial y = 0$.

The governing equations (2.1)–(2.3), are discretized on staggered grids, with the velocity variables stored at the cell faces, and pressure and density stored at the cell centres. Spatial derivatives are discretized using second-order central differencing. A low-storage third-order Runge–Kutta scheme is used for time integration. Multigrid acceleration with V cycle is used for solving the pressure Poisson equation. Smoothing of the pressure field in the multigrid procedure after the prolongation

Case	$Ri_{b,0}$	t_f	$Ri_{b,f}$	Re_f	$Re_{\lambda,f}$	$Fr_{h,f}$	$(w/u_h)_f$
A0	0.0	65	0.0	4309	70.51	-	0.718
A1	0.056	82	1.627	3652	132.34	0.203	0.310
A2	0.113	82	3.457	3763	189.33	0.159	0.231
A3	0.283	81.2	8.920	3823	266.4	0.112	0.140
A4	0.567	81.3	21.18	4166	314.42	0.0761	0.0867
A5	1.132	79.8	46.00	4341	281.95	0.0530	0.0548

TABLE 1. Description of the different simulation cases and some related parameters and bulk quantities. Subscripts 0 and f are used to denote the initial and final values. t_f denotes the final non-dimensionalized time until which the flow has been simulated, while $Ri_{b,f}$, Re_f, $Re_{\lambda,f}$, $Fr_{h,f}$, and $(w/u_h)_f$ are the final values of bulk Richardson number, Reynolds number, microscale Reynolds number, horizontal Froude number, and ratio of vertical to horizontal r.m.s. velocity. The definition of $Re_\lambda = \mathscr{U}\lambda/\nu$ is a factor of $\sqrt{3}$ smaller than the alternative that uses $q = \sqrt{2K}$ instead of $\mathscr{U}$.

and interpolation operations is done using the Gauss–Seidel method. Successive over-relaxation (SOR) with Chebychev acceleration is used as the pressure solver on the fine grid. The advection CFL number equal to 0.5 controls the time step, while the diffusion number is 0.05. Unstratified results obtained here agree well with those of Rogers & Moser (1994) and the low-Mach-number simulations of Pantano & Sarkar (2002) which, in turn, have been validated against experimental data on turbulence statistics and shear layer growth rate.

The different cases simulated and some of the related initial and final quantities are given in table 1. For all the cases, the size of the computational box is $[L_x \times L_y \times L_z] = 107.5 \times 64.5 \times 32.25$, length being non-dimensionalized with the initial vorticity thickness. The number of nodes in the x-, y- and z-directions, $N_x \times N_y \times N_z$ is $640 \times 384 \times 192$ (approximately 47 million grid points) with a uniform grid spacing, $\Delta x = \Delta y = \Delta z$. The adequacy of the chosen grid resolution is demonstrated in the Appendix through spectra and comparison with an additional simulation having half the vertical grid spacing. The same initial velocity field is used in all the simulations. The important parameters are the initial Reynolds number Re_0, initial bulk Richardson number $Ri_{b,0}$ and Prandtl number Pr. The values of $Re_0 = 681$ and $Pr = 1$ are kept constant between cases. The value of N^2 is varied keeping ΔU and $\delta_{\omega,0}$ constant, and thus the value of $Ri_{b,0}$ also varies.

The shear layer spreads in the cross-stream y-direction and with time, t. The flow statistics are also functions of y and t. Quantities such as Re and Ri_b, defined using integrated or maximum (minimum) values, change only with time and serve as indicators of the overall state of the flow. The final Reynolds number, Re_f, given in table 1 along with the broadband initial fluctuations is large enough for turbulent flow (Rogers & Moser 1994). The final Richardson number, $Ri_{b,f}$, becomes quite large and the corresponding horizontal Froude number, $Fr_h = u_h/N\delta_\omega$, becomes small. The vertical velocity becomes significantly smaller than the horizontal one as shown by the ratio of w and $u_h = \sqrt{u^2 + v^2}$ in table 1. The microscale Reynolds number is defined by

$$Re_\lambda = \frac{\mathscr{U}\lambda}{\nu} = K\sqrt{\frac{20}{3\nu\epsilon}}. \tag{2.10}$$

Here, $\mathscr{U} = \sqrt{2K/3}$ denotes a characteristic fluctuation velocity, defined using K, the turbulent kinetic energy. λ denotes the Taylor microscale defined by $\epsilon = 15\nu\mathscr{U}^2/\lambda^2$,

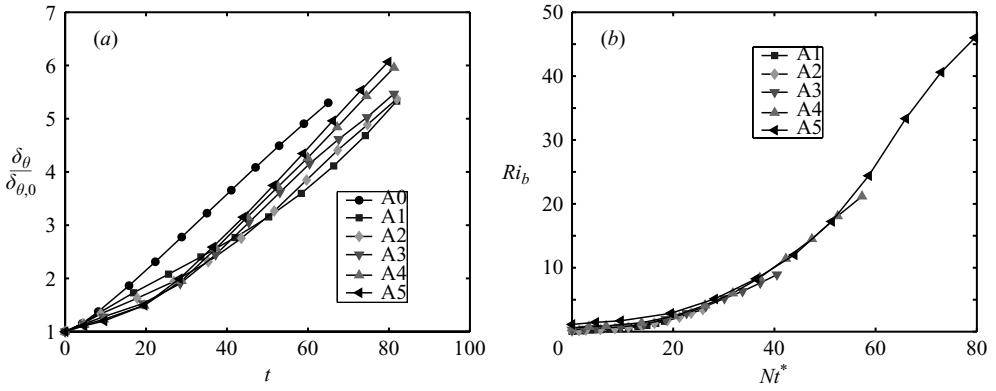

FIGURE 2. (*a*) Momentum thickness plotted as a function of time. (*b*) Variation of the bulk Richardson number as a function of normalized time, Nt^*.

with $\epsilon = 2\nu\overline{s'_{ij}s'_{ij}}$ denoting the turbulent dissipation rate. The large value of final Re_λ in the stratified cases is due to the decreased dissipation, ϵ.

3. Evolution of the mean flow

The velocity profile thickens in the cross-stream direction with increasing time. The evolution of the momentum thickness in figure 2(*a*) shows that the unstratified shear layer grows almost linearly with time. For the stratified cases, the initial growth of δ_θ is smaller, however cases A3–A5 with large N show an increased growth rate at later times when, as will be seen in §4, the KH rollers are more organized. Since $\delta_\theta(t)$ increases and ΔU is fixed, the mean shear decreases. Correspondingly, the bulk Richardson number, $Ri_b(t)$, grows, reaching greater values for larger initial Ri_b. At late time $\delta_\theta \propto t$ and, since $\delta_\omega \propto \delta_\theta$, equation (2.5) implies quadratic growth, $Ri_b \propto (Nt)^2$. The $Ri_b(Nt)$ curves in figure 2(*b*) are similar at late time, and $Ri_b > 0.5$ suggests the eventual dominance of stratification in all cases.

4. Structure of the vorticity field

Differences in the vorticity evolution owing to stratification are illustrated by comparing the unstratified case A0, moderately stratified case A2, and strongly stratified case A5. Slices of the vorticity field at a central horizontal plane ($z = 12.7$), e.g. figure 3(*a*), and a central vertical plane ($y = 25.7$), e.g. figure 3(*b*), are shown. The x and z locations are in the units of the axes in the visualizations; in these units, $\delta_{\omega,0} = 0.8$. The magnitude of the vertical (primary) vorticity, $|\omega_z|$, is used to show the overall structure of the flow. The horizontal component, $\omega_h = \sqrt{{\omega_x}^2 + {\omega_y}^2}$, is the secondary vorticity associated with three-dimensional instabilities and turbulence. The organization of vertical shear, $\sqrt{(\partial u/\partial z)^2 + (\partial v/\partial z)^2}$, is similar to that of ω_h and will not be discussed separately.

4.1. *Unstratified case A0*

In the unstratified case, the organization of vorticity is weak. The vortex structures at late time are quite complex and different from those in the transition to turbulence from infinitesimally small disturbances. Although the horizontal slice ($z =$ constant) in figure 3(*a*) shows evidence of discrete lumps of vertical vorticity which grow in time,

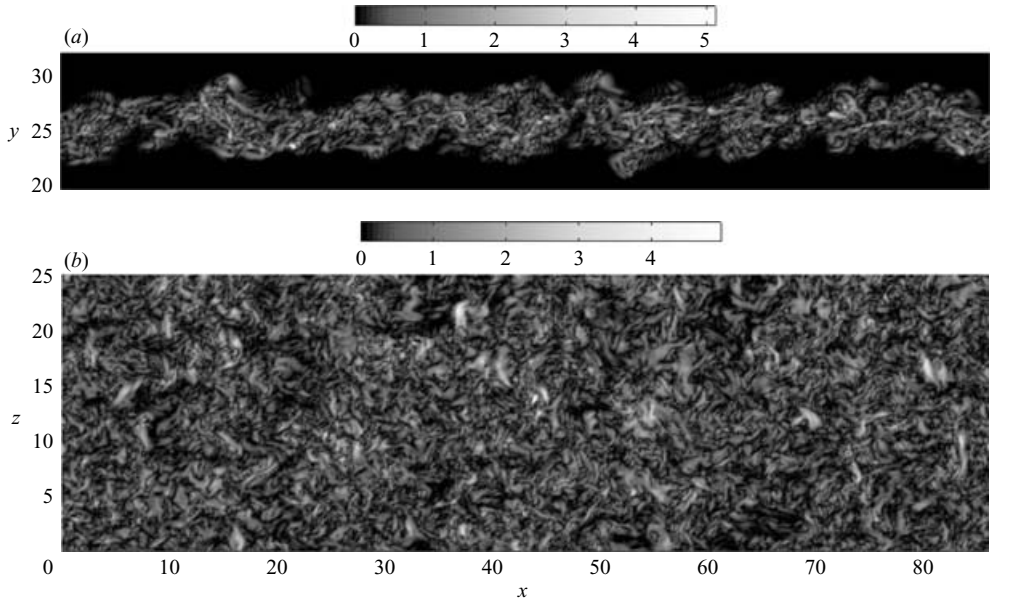

FIGURE 3. Unstratified case A0: (*a*) vertical vorticity, $|\omega_z|$, at $t = 64.8$ on a horizontal cut at $z = 12.7$, (*b*) $|\omega_z|$ at $t = 64.8$ on a vertical cut at $y = 25.7$. The grey-scale scheme here and in following figures is such that black corresponds to the minimum value and white to the maximum.

the core and braid zones are not distinct. The vertical slice, figure 3(*b*), indicates that ω_z is not coherent over significant vertical (spanwise) distances. The horizontal vorticity, ω_h (not plotted), exhibits no distinct spatial organization. Peak ω_h is somewhat larger than peak ω_z indicating strong three-dimensionality that progressively increases with increasing *Re*. The weak organization of the vorticity field observed here in case A0 is consistent with the DNS results of Rogers & Moser (1994) for their case TBL that started with a turbulent boundary layer with peak $q/\Delta U = 7.5\%$. Additional strong two-dimensional forcing, approximately ten times the three-dimensional fluctuation energy, was found necessary by Rogers & Moser (1994) to maintain spanwise-coherent rollers at late time.

4.2. *Moderate initial stratification, case A2 with* $Ri_{b,0} = 0.113$

The vorticity field in the intermediately stratified case A2 shows significantly more organization than case A0. From the incoherent initial conditons, KH rollers and interspersed braids appear as seen in figure 4(*b*), becoming more distinct in the later panels. The cores thicken by amalgamation and the braid regions thin by exuding vorticity until $t \simeq 52$ after which dynamics similar to the transitional low-*Re* shear layer studied by Winant & Browand (1974) is seen, although the *Re* here is larger. For example, co-rotation of vortex cores and their pairing is evident later in time as in the evolution of the region around A from $t = 51.7$ to $t = 82$. Accompanying this pairing event is the stretching of the vertical vorticity in the vicinity of B that results in a thin braid at $t = 82$. More complex vortex interactions can also be seen. The region between C and E at $t = 51.7$ has about six emerging structures which interact to finally give rise to three non-equispaced vortex cores. The vorticity lump at D appears to be stretched and torn by its interaction with the neighbouring vorticity,

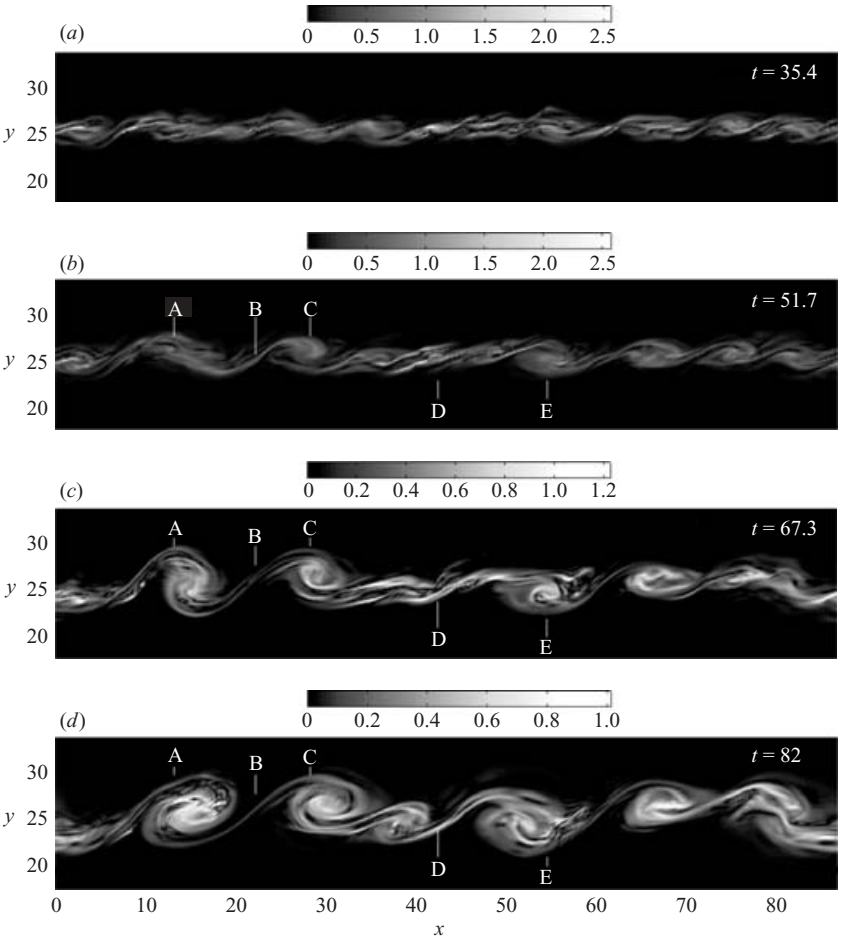

FIGURE 4. Vertical vorticity magnitude in case A2 on a horizontal central plane, $z = 12.7$, at different times. From top to bottom, $t = 35.4$, 51.7, 67.3, and 82. The corresponding values of Richardson number are $Ri_b = 0.68$, 1.32, 2.25 and 3.46. Multiply t by 0.224 to obtain Nt^*.

eventually becoming a thin distinct braid by $t = 82$. The vorticity in the vicinity of C and E amalgamates to form thick vortex cores at $t = 82$ without showing the clear co-rotation and pairing seen in the vicinity of point A.

Columnar cores of $|\omega_z|$ emerge from the initial broadband fluctuations, a remarkable difference with respect to unstratified case A0. The formation of the vortex columns and their evolution is shown in figure 5. The region between $x = 70$ and $x = 85$ in figure 5(a, b) shows two vortex cores that approach and overlap in the central region, somewhat similar to the so-called helical pairing observed by Chandrsuda *et al.* (1978) and Comte *et al.* (1992). The central region between $x = 40$ and $x = 60$ shows the emergence of three vortex cores at $t = 51.7$. At $t = 64.8$, the left member (centred at $x = 40$) of this trio moves toward the middle one (centred at $x = 48$) in a spanwise non-uniform fashion and, similarly, the right member is also drawn in. At $t = 82$, the three members have paired to result in a 'branched' vortex. The central portion ($10 < z < 15$ and $45 < x < 55$) forms a single vortex core with its right and left sides rotated out of the plane, while above and below are two branches. The vortex lines in the left, bottom branch pass through the central portion and connect to the left, top

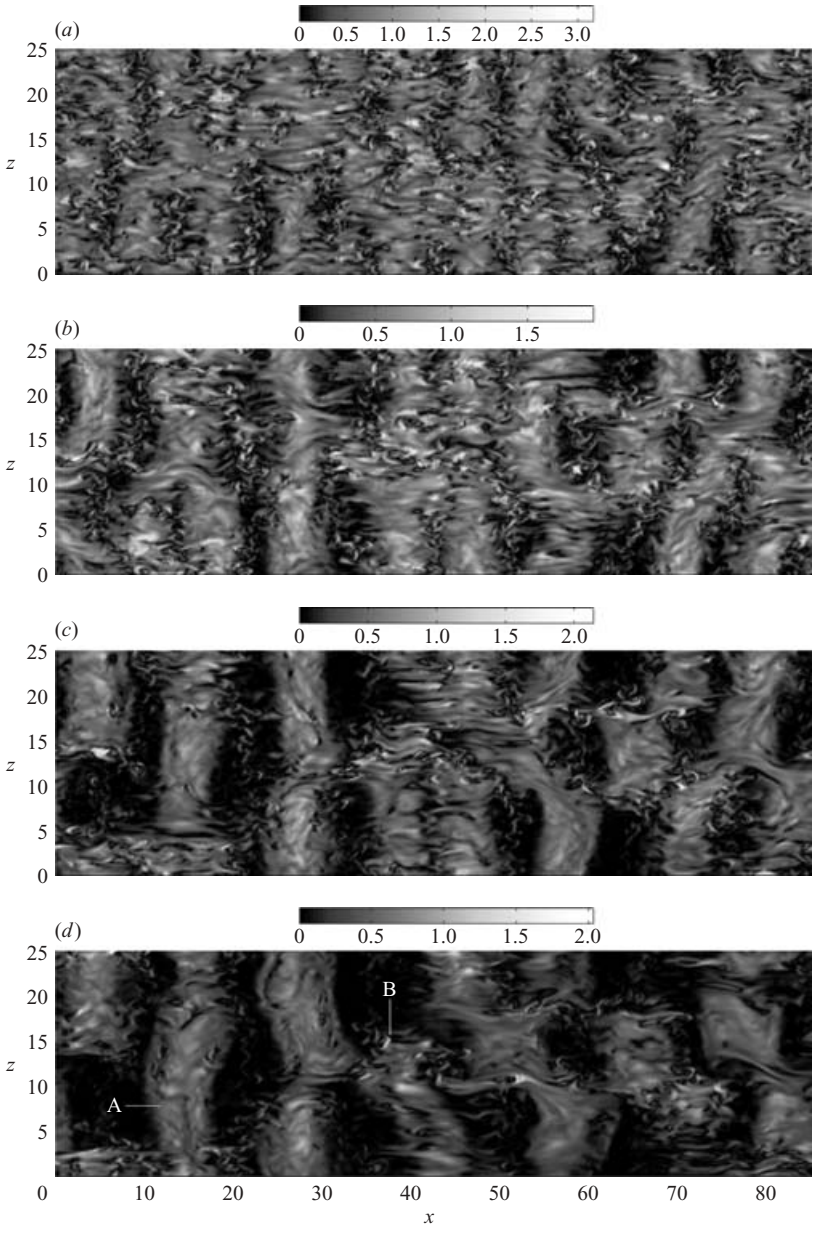

FIGURE 5. Vertical vorticity magnitude in case A2 on a vertical central plane, $y = 25.7$, at different times. From top to bottom, $t = 35.4$, 51.7, 67.3 and 82, and correspondingly, $Ri_b = 0.68$, 1.32, 2.25 and 3.46.

branch with a similar connection between the right branches. At late time, figure 5(*d*), the columnar cores tend to align parallel to the z-axis, having small inclination with the vertical. The column around point A extends throughout the vertical extent of the domain while the column at point B is 'truncated' to form a 'dislocation' in ω_z. The dislocations will be more distinct in case A5, discussed later.

Although staggered rollers have also been seen to form in unstratified shear layers due to local spanwise pairings triggered by low-amplitude disturbances, there is a

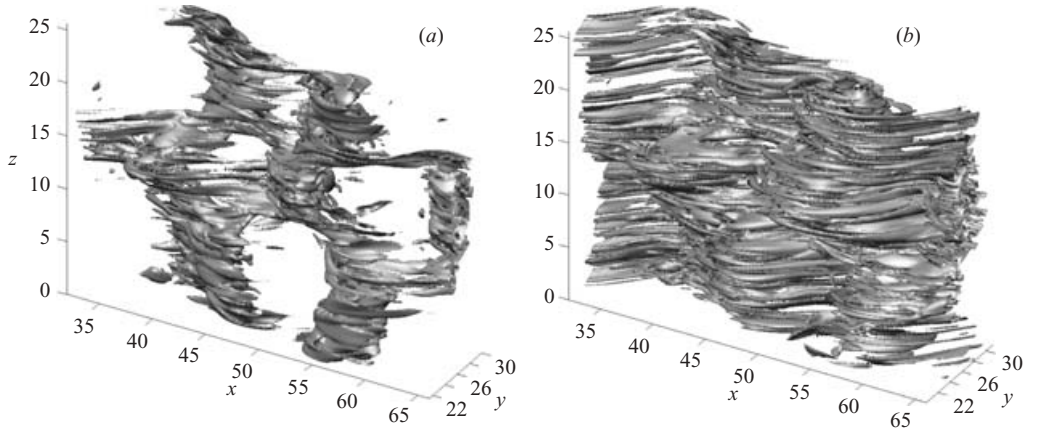

FIGURE 6. Case A2, three-dimensional isosurface of (*a*) the $|\omega_z|$ field and (*b*) the ω_h field at time $t = 82$. Isosurface value $= 0.4$.

significant difference with respect to the local pairings observed here. In the unstratified shear layer, Nygaard & Glezer (1994) and Collis *et al.* (1994) study local pairing triggered by a controlled local phase shift of the spanwise vortices in the initial conditions and find the emergence of a 'diamond' vortex lattice. The detailed numerical simulations by Collis *et al.* (1994) reveal that, after the vortex cores approach each other locally, there is a mutually repulsive velocity field induced by the convoluted core and rib vortices in that region that tends to decouple the cores so that the actual zone of vortex pairing is relatively small compared to the total spanwise extent of the rollers. In the stratified case, the pairing zone has smaller ω_h which allows the pairing to proceed to completion and there is no evidence of decoupling of the paired rollers with time. Furthermore, the regions away from the local pairing are quasi-vertical instead of being strongly inclined and, depending on the details of the later-time evolution, can interact with other structures.

The horizontal vorticity, ω_h, has also been examined and its peak value found to mainly occur in overturning braid regions between the columnar cores of ω_z. It is known that the braid region between adjacent KH rollers, when subject to the strain field induced by the rollers, is strongly susceptible to three-dimensional instabilities (Pierrehumbert & Widnall 1982; Moser & Rogers 1993; Lasheras, Cho & Maxworthy 1986; Lasheras & Choi 1988). In the case of discrete, deterministic initial conditions, the braid vorticity is initially organized, e.g. streamwise counter-rotating rib vortices and hairpins have been observed; these later break down into a complex three-dimensional vortical field. In the present case, chaos-to-order, the rollers emerge from an initially complex disorganized vorticity field and distinct streamwise-coherent rib vortices are not observed. The ω_h field has thin 'horizontal' striations that become more pronounced with time.

That $|\omega_z|$ organizes into interacting columnar vortex cores and ω_h into striations is made more clear by a three-dimensional perspective. Figure 6(a, b) shows an isosurface of $|\omega_z|$ and of ω_h in the region between $x = 32$ and 66, at $t = 82$. The horizontal meandering of the vortex cores is clearly evident in figure 6(*a*). The lower part of the structure at $x = 42$ actually consists of two merging vortex cores. The spanwise coherence of this structure is truncated near $z = 15$, where ω_z branches out to locally merge with adjacent columns. A single column of ω_z forms again near $x = 45$, above $z = 17$ and continues to the top of the domain, which is in turn

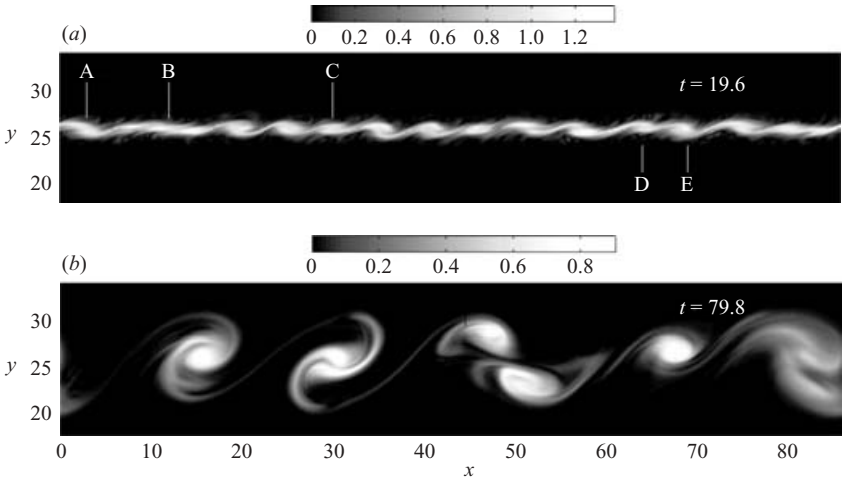

FIGURE 7. Case A5, spanwise vorticity magnitude, central z-plane, $t = 19.6$, and $t = 79.8$.

connected to the bottom of the domain through periodicity. The column in the bottom region of figure 6(a), near $x = 55$, meanders to the left near $z = 15$ and merges locally with the adjacent roller. This vortex column is also seen to interact locally with the vortex column to its right. Thus, a staggered lattice of spanwise vorticity columns tends to form. The horizontal vorticity in figure 6(b) is organized into thin, horizontally aligned strips. Some of the ω_h structures are located in the rollers while most of them are wound around the skeletal framework formed by the ω_z rollers.

To summarize, the DNS shows that the vorticity field in case A2 is much more organized relative to case A0. This is a consequence of horizontal vorticity being suppressed by stratification which resists the induced overturning vertical motion. As discussed in the introduction, secondary vorticity, the component ω_h in this flow, has been found to be crucial to the 'mixing transition' of the unstratified case. The weakening of ω_h causes the reverse phenomenon whereby the fundamental KH instability regains importance later in time. The emerging cores of ω_z are columnar, prevented by stratification from having large-scale deviations from the vertical observed in the unstratified case (Lasheras & Choi 1988; Moser & Rogers 1993) since that would result in significant vertical transport. The columns of ω_z form a staggered lattice, a feature that is more distinct in case A5 as discussed below in §4.3.

4.3. *High stratification, case A5 with* $Ri_{b,0} = 1.132$

The coherent structures of ω_z are visually sharper in case A5 relative to case A2 as is readily seen by comparing figure 7(b) with figure 4(d) at similar t. Another difference is that distinct core and braid structures are formed earlier in case A5 than in case A2 and are therefore thinner. At $t = 19.6$, about 14 rollers can be identified which agrees well with the domain size in x containing 14 to 15 of the most unstable wavelength of the KH instability. When N is used for normalization of dimensional time, t^*, coherent vortex cores appear at similar time, $16 < Nt^* < 20$ in cases A2–A5, and the corresponding stratification level is $1.25 < Ri_b < 2.25$. The paired KH rollers, for example at $x = 30$ and $x = 50$ in figure 7(b), show the strong co-rotation characteristic of quasi-two-dimensional vortex dynamics, a feature that was not prominent in case A2.

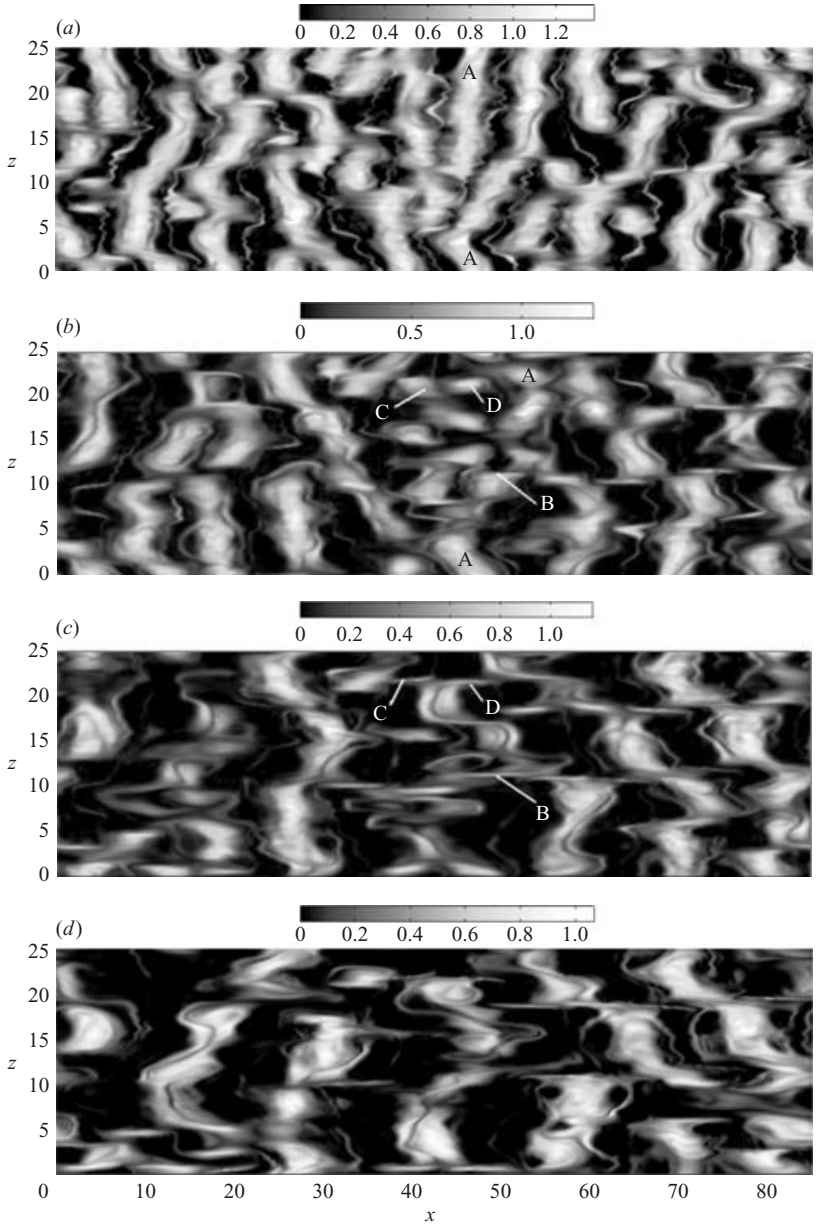

FIGURE 8. Case A5, spanwise vorticity magnitude, $|\omega_z|$, central y-plane. $t = 36.5$, 51.5, 66.1, 79.8. t and Nt^* have the same numerical values in this case. $Ri_b = 2.87$, 8.27, 17.24, 33.35, and 46.

Similar to case A2, there is formation of columnar cores in case A5 as shown by the vertical cut of $|\omega_z|$, figure 8. These cores become distinct at smaller t but similar buoyancy time, $16 < Nt^* < 20$. Initially, long continuous structures, inclined to the vertical, are formed, e.g. AA in figure 8(a). That buoyancy tilts segments of the vortical cores will be shown later in § 5. Local interactions of these tilted segments with their neighbours modifies the initially continuous vortex core to form a set of locally vertical structures. Figure 8(b) shows that the previously continuous structure

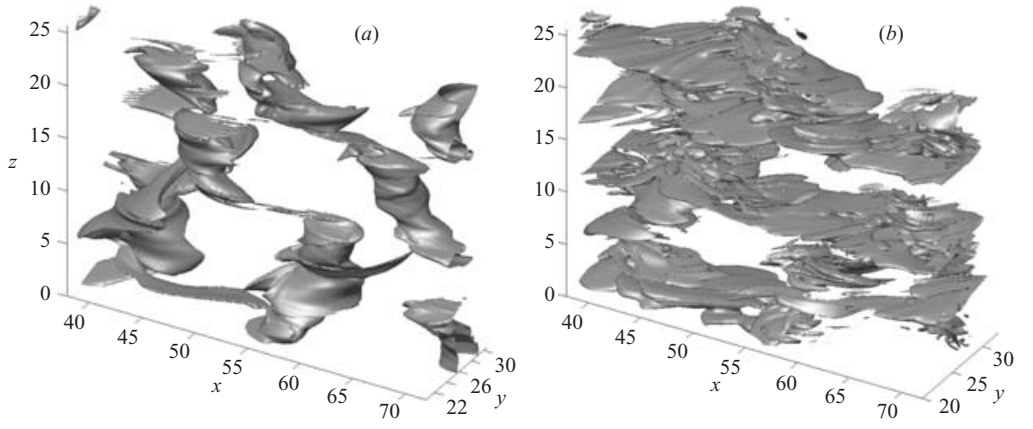

FIGURE 9. Case A5, three-dimensional structure of (*a*) the $|\omega_z|$ field and (*b*) the ω_h field at time $t = 79.8$. Isosurface value $= 0.4$.

AA has evolved to form a set of stubby vertical structures by relative horizontal sliding, e.g. at B. Short vortex structures, e.g. C and D, collapse with increasing time. Eventually, the vorticity field develops thin *dislocations*, marked in figure 8(*c*).

Similar to case A2, the horizontal vorticity, ω_h, is reduced by stratification and has a striated appearance. However, there is an important difference at the end of the simulations: peak ω_h occurs at the braids in case A2 and progressively decreases with time, while peak ω_h in case A5 occurs at the dislocations and increases with time. This difference could be because the final $Nt^* = 25.2$ is not sufficiently large in case A2; in case A5, the final value was $Nt^* = 79.8$.

Thus, the vorticity at late time in case A5 organizes into a dislocated lattice of quasi-vertical cores of ω_z with ω_h concentrated in thin sheets at the dislocations. The visualization of an isosurface of $|\omega_z|$ and of ω_h between $x = 38$ and 72 in figure 9 illustrates this three-dimensional topology of the coherent structures. Comparison with a similar visualization, figure 6, shows the following differences in case A5 with respect to A2: the vortex cores are smoother, braid vortex tubes of ω_h are absent, and dislocations of vortex cores with associated sheets of ω_h are present. We reiterate that the rectangular lattice of vortex cores observed in cases A5 and A2 is different from lattices observed in the transitional stage of unstratified shear layers, the hexagonal lattice of Comte *et al.* (1992), and the diamond lattice of Nygaard & Glezer (1994) and Collis *et al.* (1994).

5. Structure of the density field

The structural organization of the density field and its interaction with the organized vorticity field are described in this section. Case A5, where buoyancy effects are prominent from early on, is discussed in detail.

5.1. *Core structures*

The density field is organized and strongly coupled to the organized vorticity field as illustrated by figure 10(*a–d*). After an initial transient when random small-scale density fluctuations form, significant ρ' occurs mainly within the cores, for example, A and B in figure 10(*a*, *b*), as well as C1, D1, and E1 of figure 10(*b*). Vortex cores with the following types of density organization are seen: (i) inclined structures with heavier (red) and lighter (blue) fluid being side-by-side, and (ii) vertical structures with lighter

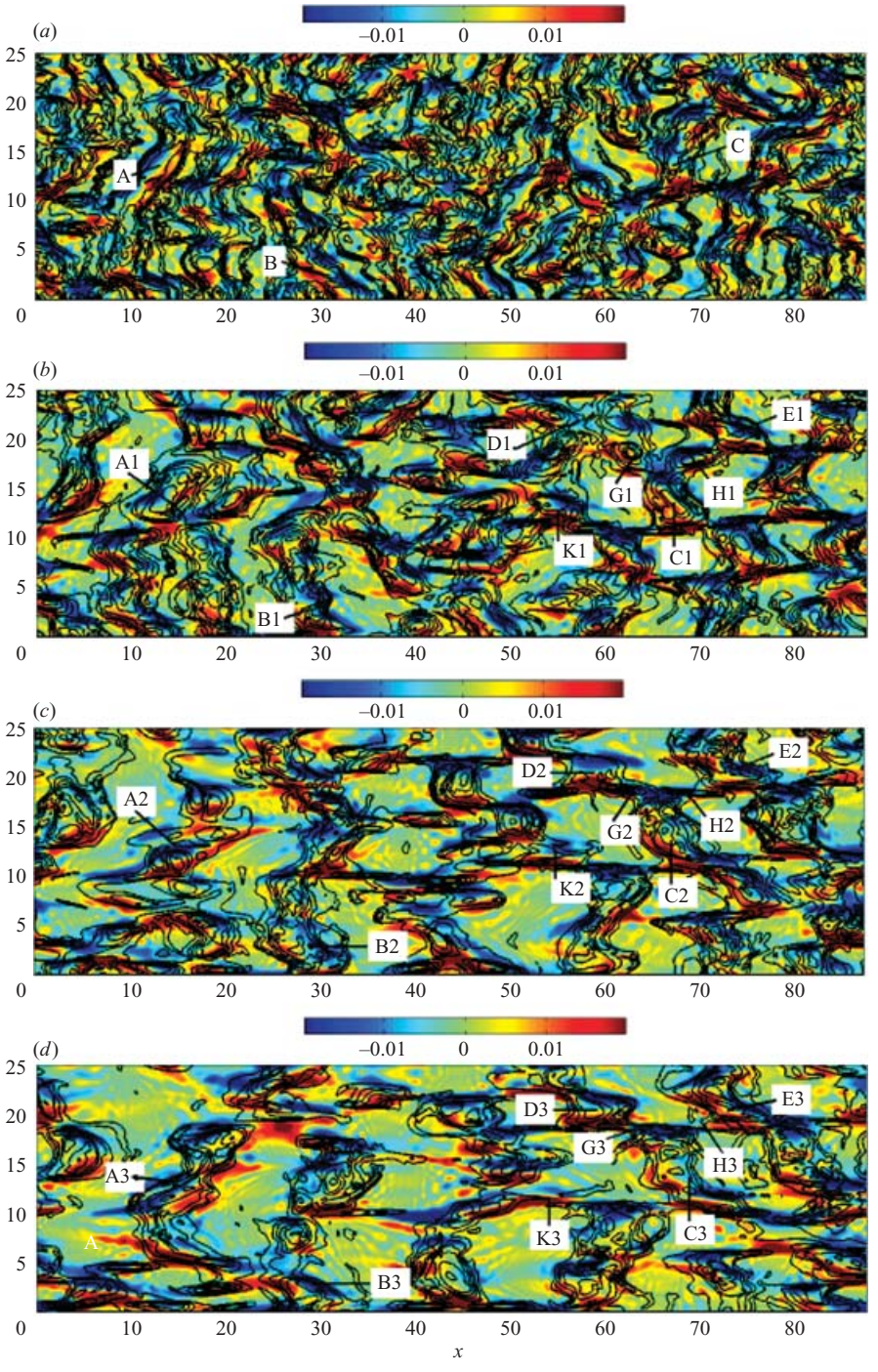

FIGURE 10. Density perturbation (red indicates heavier than ambient fluid, $\rho' > 0$, and blue indicates lighter fluid with $\rho' < 0$) for case A5 with overlapping ω_z contours in black, centre y-plane, (*a*) $t = 36.5$, (*b*) $t = 51.5$, (*c*) $t = 66.1$, (*d*) $t = 79.8$. Specific structures are shown in the panels using a numerical suffix which increases with time.

fluid directly over heavier fluid. A and B in figure 10(*a*) are examples of inclined vortex cores, tilted to the right and left, respectively, with high-ρ' below low-ρ' fluid in both. The angle of inclination generally increases with time bringing the lighter fluid above the heavier fluid. K1–K3 and D2–D3 are examples of vertical cores with a stable arrangement of heavier under lighter fluid. Figure 11 is an expanded view of a subsection of figure 10(*c*). That the structure with negative ρ' (blue) overlying positive ρ' (red) is associated with a vortex core is very clear in D2. The superposed isopycnals show that the lighter fluid in D2 is associated with a downward dip of the isopycnals and the heavier fluid is associated with an upward bulge of the isopycnals. Such convergence of isopycnals towards the centre of a vortical structure is similar to that observed in pancake vortices by Beckers *et al.* (2001) and Godoy-Diana & Chomaz (2003).

Inclined vortex cores are explained with a schematic, figure 12(*a*), showing adjacent heavy and light fluid, an unstable density contrast, that tilts the vortex core to the right owing to baroclinic torque. The isopycnals on the right of the vortex core are displaced upward to give $\rho' > 0$; similarly $\rho' < 0$ at the left is due to downward isopycnal displacement. Careful comparison between the density and the vorticity in case A5 shows that the tilting of vortex cores is almost always towards the direction of the heavy fluid.

Quasi-vertical, finite-size vortex cores with negative ρ' overlying positive ρ', observed in the DNS, can be explained using the idealization of figure 12(*b*), which shows an isolated vortex core of radius R and height H with axisymmetric azimuthal velocity $v_\theta(r, z)$, and $v_r = v_z = 0$. Under these assumptions, the radial momentum equation simplifies to a centrifugal balance,

$$\frac{\partial p}{\partial r} = \rho_0 \frac{{v_\theta}^2}{r}. \tag{5.1}$$

Integrating radially shows that the pressure external to the vortex, p_0, is larger than at the centre A. The vertical velocity is small at late time and neglecting its contribution to the vertical momentum equation gives

$$\frac{\partial p}{\partial z} = -\rho' g, \tag{5.2}$$

where p is the deviation from the hydrostatic pressure. The result of (5.1) that $p_0 > p_A$ is one that can be satisfied by the hydrostatic balance (5.2), if $\rho' < 0$ in the upper half of the vortex, i.e. the isopycnal dips down from above to bring lighter fluid from the stratified ambient. A similar integration vertically down from the centre shows $\rho' > 0$ in the lower half of the vortex. Thus, the low pressure at the vortex centre leads to isopycnal convergence.

The lattice of dislocated vortex cores, discussed in § 4.3, can now be explained in view of the observed organization of the density field. During vortex merger, if fluid of different density is brought together, the paired structure tilts sideways owing to buoyancy. The vorticity field soon consists of quasi-vertical vortex cores, see figure 12(*b*), connected by tilted vortical structures, see figure 12(*a*); for example, C1, D1 and E1 in figure 10(*b*) are connected by inclined vortices G1 and H1. The tilted structures are gravitationally unstable and collapse later in time to form dislocations. Occasionally, the vertical vortex cores can also collapse, for instance, during the evolution of vortex K in figure 10(*b*, *c*), before it merges with the adjacent tilted vortex structure at its left in figure 10(*d*).

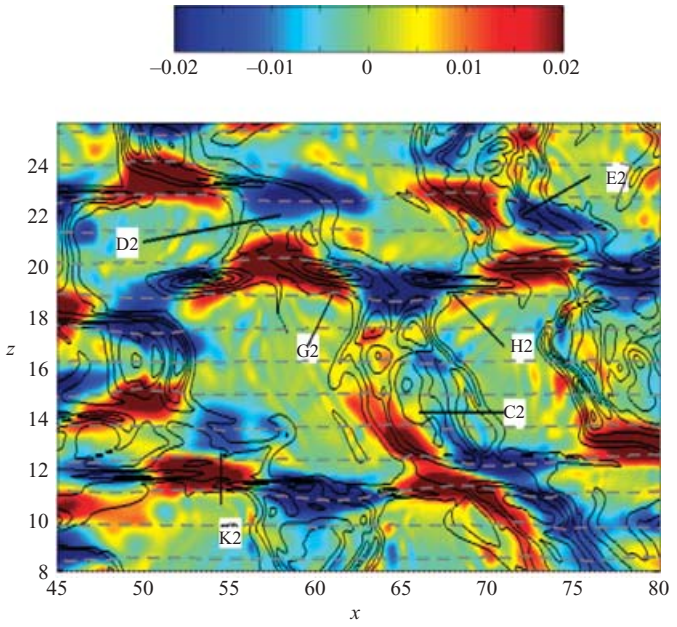

FIGURE 11. View of a subsection of density perturbation with overlapped isopycnals (dashed lines) and ω_z contours (solid lines) for case A5, $t = 66.1$, shown in figure 10(c). Vertical displacement is exaggerated.

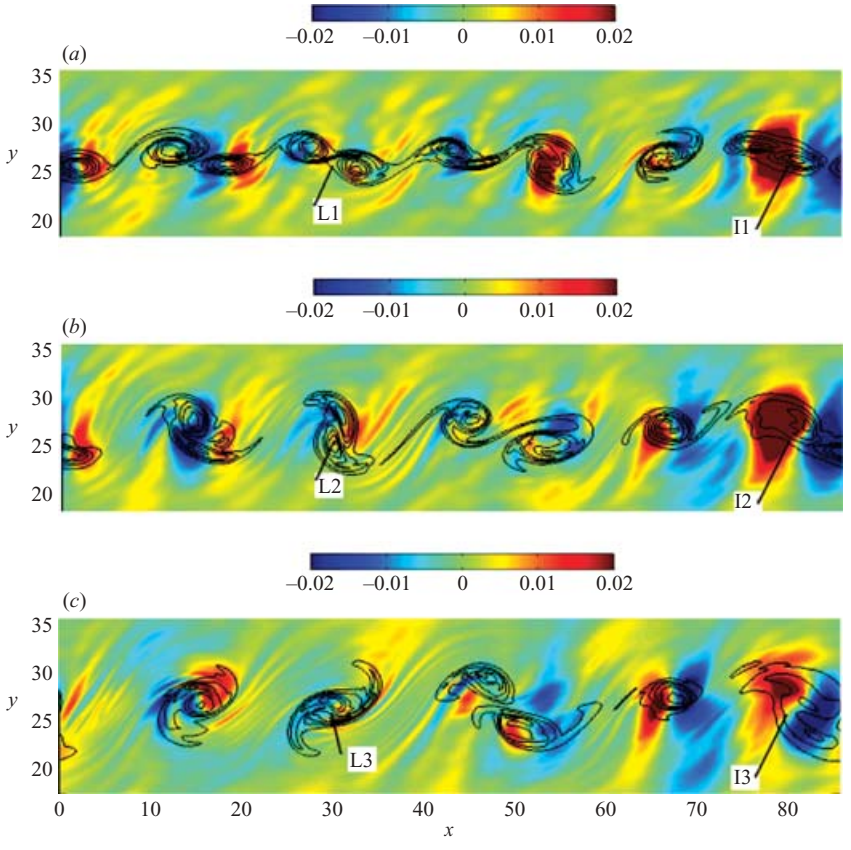

FIGURE 13. Density perturbation with vertical vorticity contours superimposed for case A5, centre z-plane, (a) $t = 51.5$, (b) 66.1, (c) 79.8. $Ri_b = 17.24$, 33.35, and 46.

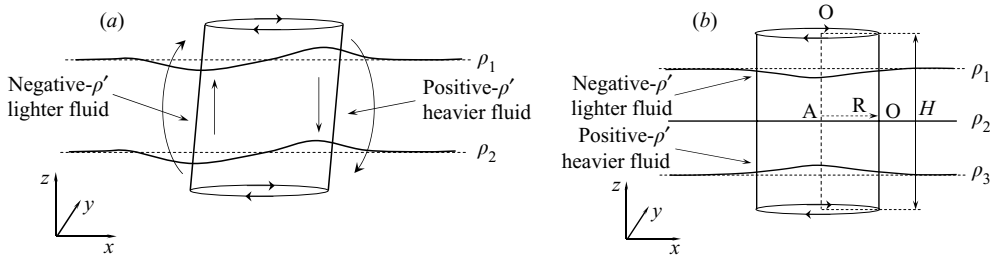

FIGURE 12. Schematic showing (*a*) tilting of the vortex rollers owing to lateral variation of density perturbations, (*b*) convergence of isopycnals toward the central low-pressure zone of a vertical vortex.

The horizontal dynamics of the vortex cores is made clear through the successive panels of figure 13. Most of the large-amplitude (red and dark blue) density variation is in the vortex cores. The vertical vorticity present at early time (not shown) in the braid region diminishes later and so does the density variation there. Interestingly, there is fine-scale density variation of smaller amplitude (yellow and light blue) in the erstwhile braid regions that appear to travel outward and to also rotate clockwise owing to the shear. This is suggestive of internal wave radiation. Merging of vortex cores is seen. The merging in L1–L3 is reminiscent of pairing seen in two-dimensional simulations of the unstratified shear layer. However, the merger in I1–I3 that brings together fluid with a large density contrast is qualitatively different owing to buoyancy. The vorticity is less compact relative to L and the heavy/light fluid also shows significant lateral spread. Zone I corresponds to the upper and lower ends of two adjacent truncated vertical vortices whose buoyancy contrast cannot be supported during vortex merger so that the fluid moves out laterally with heavy fluid sliding under light. The later-time snapshots also show regions of partially mixed fluid (yellow and light blue) that spread out from the vortex cores. These regions, with less fine-scale structure than the gravity waves radiating from the stretched braid vorticity, are associated with the intrusions discussed below in § 5.4.

The density structure of case A2 was also examined. It was found that, similar to case A5, segregated density perturbations occur and tilt vortex cores. Dislocations of the cores are also present and associated with strong distortions of the vortex lines and significant deviations of the isopycnals from their respective mean positions. More small-scale velocity and density fluctuations are present in case A2 relative to A5 because Nt^* and Ri_b are not sufficiently large. Unlike case A5, there is significant ω_h in the braid regions of case A2 which generates ρ'. Magnified visualizations of the isopycnals (not shown) reveal some small-scale overturning regions, predominantly in the braid zones, in contrast to case A5 which, at late time, exhibits no overturning of isopycnals.

5.2. *Length scales of the vortex cores*

Case A5 was simulated up to $Nt^* = 149.1$ to investigate the behaviour of length scales of the coherent vortices. Owing to the statistical jitter in the position of the vortices, the velocity and density spectra do not show distinct peaks at a specific scales and, instead, visualizations of the vorticity are used to characterize the length scales. Comparison of figure 14(*a*) with a snapshot at earlier time, figure 7(*b*), shows that the horizontal scale of the vortex cores increases owing to pairing and, correspondingly, the number of discrete vortex cores decreases. At $Nt^* = 149.1$, there is a central

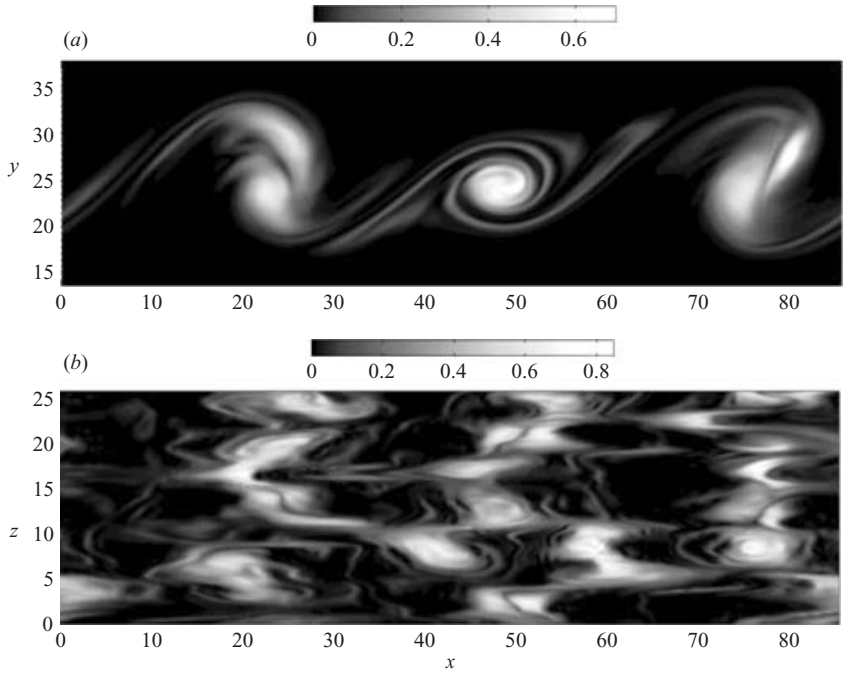

FIGURE 14. Case A5, magnitude of ω_z at $Nt^* = 149.1$: (a) horizontal cut, $z = 12.76$, (b) vertical cut, $y = 25.7$.

vortex core and two pairs of vortex cores at each side of the computational domain. A central vertical cut, figure 14(b), shows a – by now familiar – dislocated lattice of quasi-vertical vortex cores. The maximum number of vortex cores in a vertical transect is about 5, the same number found earlier at $Nt^* = 79.8$. Inspection of a movie of the evolution of ω_z shows that during merger of neighbouring (but vertically offset) sections of vortex cores, the vertical length scale of the vortex core may increase temporarily but, since fluid of different density is brought together, buoyancy effects described in the previous section operate to limit the vertical length scale. Thus, the overall horizontal size of the vortex cores increases with time while the vertical size does not, so that the initial columnar appearance of the vortices progresses towards a pancake shape.

The combination of centrifugal and hydrostatic balance leading to (5.1)–(5.2) is helpful to identify the characteristic vertical scale. Since the azimuthal velocity of the vortices is proportional to the imposed velocity difference, ΔU (5.1) simplifies to

$$p_0 - p_A \propto \rho_0 \Delta U^2. \tag{5.3}$$

The density fluctuation is associated with the vertical displacement of the external isopycnal, assumed to be proportional to the local vertical coordinate, so that integration of (5.2) from the centre to the upper edge of the vortex leads to

$$p_0 - p_A = -\int_0^{H/2} \rho' g \, \mathrm{d}z \propto -\int_0^{H/2} \frac{\mathrm{d}\bar{\rho}}{\mathrm{d}z} z g \, \mathrm{d}z = -g \frac{\mathrm{d}\bar{\rho}}{\mathrm{d}z} \frac{H^2}{8}, \tag{5.4}$$

where H is the height of the vortex. After equating the right-hand sides of (5.3) and (5.4), the following expression for H is obtained:

$$H = C_1 \frac{\Delta U}{N}, \tag{5.5}$$

where C_1 is a coefficient. Thus, the vertical extent of the vortex core, related to the buoyancy length $\Delta U/N$, becomes invariant with time if the coefficient, C_1, approaches a constant value. The DNS data of case A5 are examined and the scaling law (5.5), is found to hold at long time, from $Nt^* = 60$ until the end of the simulations at $Nt^* = 150$. The data of case A5 indicate $H \simeq 5$ while $\Delta U/N = 0.8$ giving the final expression for the vortex core height,

$$H \simeq 6 \frac{\Delta U}{N}. \tag{5.6}$$

5.3. *Vorticity transport equation*

The vorticity transport equation is examined using DNS and the importance of the baroclinic term is quantitatively demonstrated. The vorticity transport equation is

$$\frac{\partial \omega_i}{\partial t} = -u_k \frac{\partial \omega_i}{\partial x_k} + \omega_k \frac{\partial u_i}{\partial x_k} + \nu \frac{\partial}{\partial x_k} \frac{\partial \omega_i}{\partial x_k} + \epsilon_{i3k} \frac{1}{\rho_0} g \frac{\partial \rho}{\partial x_k}, \tag{5.7}$$

In (5.7), $-u_k \partial \omega_i / \partial x_k$ is the vorticity advection term, $\omega_k \partial u_i / \partial x_k$ denotes vortex stretching/tilting, $\nu \partial^2 \omega_i / \partial x_k^2$ denotes vorticity diffusion, and $\epsilon_{i3k} (g/\rho_0) \partial \rho / \partial x_k$ is the baroclinic term (often called baroclinic torque) which directly couples the buoyancy and vorticity fields.

Terms in the evolution of a horizontal vorticity component, ω_y, are discussed first. The baroclinic term, $(1/\rho_0) g \partial \rho / \partial x$, in a vertical central cut is visualized in figure 15(*a*). If positive, the baroclinic term results in clockwise motion and vice versa. Comparison with figure 10(*c*) shows that continuous positive (negative) streaks of $(1/\rho_0) g \partial \rho / \partial x$ are associated with high-ρ' fluid situated to the right (left) of low-ρ' fluid; A, B and C in figure 15(*a*) are incipient dislocations while D, E and F are inclined vortex cores. The baroclinic term is always positive in regions where ω_z is tilted rightward and negative in structures tilted toward the left, further corroborating the statement in § 4 that density perturbations act to tilt sections of vortex cores in case A5. The minimum and maximum values of $(1/\rho_0) g \partial \rho / \partial x$ at the centre y-plane in code units are -0.537 and 0.535, respectively, with the variance being 0.089. The vortex tilting term, $\omega_z \partial v / \partial z$, that produces ω_y by tilting of ω_z columns, is shown in figure 15(*b*). It is observed that vortex cores tilted to the right generate negative $\omega_z \partial v / \partial z$, as shown at location A, while cores tilted leftward generate positive $\omega_z \partial v / \partial z$ as at B. The observed sign of $\omega_z \mathrm{d}w/\mathrm{d}z$ thus implies that, in the inclined vortex core, the vortex tilt term resists the baroclinic torque, and can be explained as follows. The primary vortex cores in the shear layer have a clockwise spin (positive v on the left side and negative v on the right side), see axes in figure 1. Any tilt of the vortex core axis from vertical to its right (left) would then create a positive (negative) $\partial v / \partial z$. Since the clockwise spin implies that ω_z is negative, the vortex tilt term, $\omega_z \partial v / \partial z$, is negative (positive) in a vortex core tilted to the right (left). The minimum and maximum values of $\omega_z \partial v / \partial z$ are -0.502 and 0.597, respectively, with the variance being 0.0687. The vortex tilting terms are particularly intense in the dislocation zones (C, D) where the vertical shear is large. The baroclinic term is clearly of similar order as vortex tilting, thereby underscoring the importance of buoyancy to vorticity dynamics in this flow. Inspection of the ω_y equation at various times indicates that baroclinicity triggers the

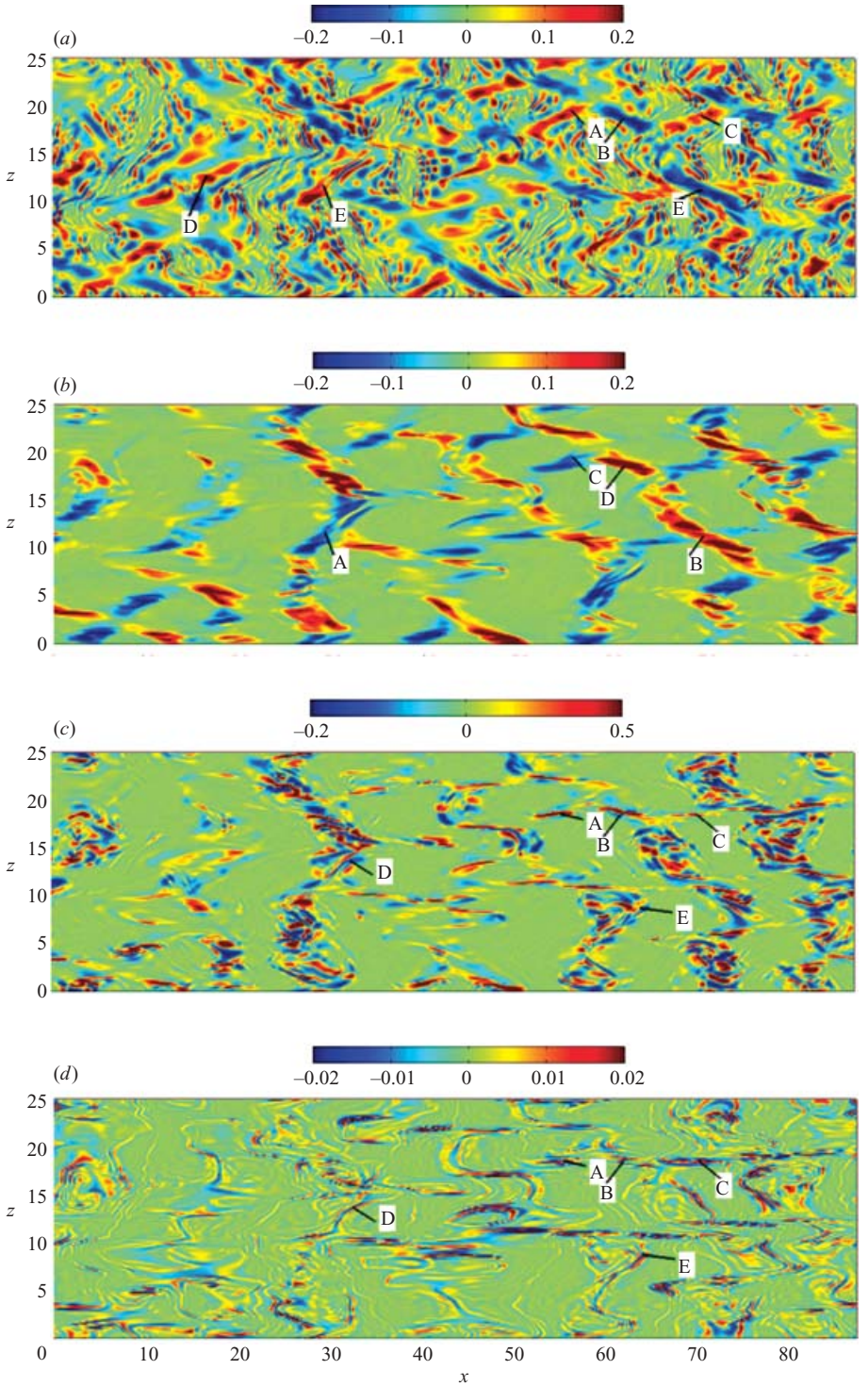

FIGURE 15. Different components of the vorticity transport equation for case A5, centre y-plane, $t = 66.1$, (*a*) $(1/\rho)g\partial\rho/\partial x$, (*b*) $\omega_z \partial v/\partial z$, (*c*) $\omega_z \partial w/\partial z$, and (*d*) $\nu\nabla^2\omega_z$.

initial inclination of vortex cores. The viscous diffusion term (not shown) peaks at the dislocations and edges of the vortex cores, becoming comparable to the vortex tilt and baroclinic terms. The balance in the equation for ω_x is similar to that for ω_y and is not discussed further.

Assessment of the transport equation for ω_z shows that advection by horizontal velocity is the largest term; the minimum and maximum values are -0.505 and 0.76 respectively, with the r.m.s. being 0.0476. Figure 15(*c*) shows $\omega_z \partial w/\partial z$, the vertical stretching/compression of ω_z. Negative $\omega_z \partial w/\partial z$ that results from stretching the vortex cores (containing mainly negative ω_z) strengthens them, while positive $\omega_z \partial w/\partial z$ resulting from compression weakens them. Large positive $\omega_z \partial w/\partial z$ is observed at dislocation zones, e.g. A, B, C, where the vertical vorticity collapses. Regions of both positive and negative $\omega_z \partial w/\partial z$ are observed in the truncated core regions associated with local stretching and collapse of vorticity. The minimum and maximum values of $\omega_z \partial w/\partial z$ are -0.248 and 0.1532, with the r.m.s. being 0.0186. Figure 15(*d*) shows diffusion of ω_z which is observed to be mainly concentrated in the dislocation zones, e.g. A, B, C, and the edges of the vortex cores, e.g. D, E. The intensity of ω_z diffusion is comparable to vortex stretching, with minimum and maximum values at the central y-plane of -0.056 and 0.104, and r.m.s. value of 0.0058.

Evaluation of the vorticity transport equation shows that, at the thin dislocations, the two dominant terms are vortex stretch/tilt and diffusion. In the case of ω_z, equating these two terms, namely $\omega_z \partial w/\partial z$ and $\nu \partial^2 \omega_z/\partial z^2$, gives the following estimate of the thickness, l_d, of the dislocations: $l_d \propto \sqrt{\nu/a}$ where a is the characteristic compressive strain rate. A similar consideration of the balance of ω_x or ω_y gives $l_d \propto \sqrt{\nu/s}$ where s is the characteristic vertical shear. We find that the r.m.s. vertical shear (or strain) in the stratified cases is proportional to N giving $l_d \propto \sqrt{\nu/N}$. The quantity $\sqrt{\nu/N}$ is the so-called primitive scale that appears in stratified turbulence literature, for example, Gibson (1980) and Barry *et al.* (2001). In energetic thermally stratified turbulence, Barry *et al.* (2001) find that the r.m.s. turbulence length scale, $\overline{T'^2}/\mathrm{d}\bar{T}/\mathrm{d}z$, is approximately $20\sqrt{\nu/N}$. Examination of the DNS data shows that approximately 4 points of the computational grid span a dislocation vertically; thus, the dislocation thickness is

$$l_d \simeq 15\sqrt{\frac{\nu}{N}}\,. \tag{5.8}$$

5.4. *Edge dynamics*

The edges of the shear layer, devoid of strong ω_z, cannot sustain regions with density fluctuations which then collapse. Downward moving tongues of fluid with higher density often encounter upward moving low-density tongues and these combined structures propagate laterally as *intrusions*. Intrusions begin to form at $Nt \simeq 10$, close to the value $Nt = 9.6 \pm 2.5$ reported by Browand *et al.* (1987). The underlying mechanism is shown by the schematic, figure 16, inspired by previous investigations of the collapse of stratified turbulent fronts by Browand *et al.* (1987), Liu *et al.* (1987), Thorpe (1982), and Ivey & Corcos (1982). Squeezing of fluid in the vertical direction accompanied by its horizontal spread is also observed in a collapsing isolated region of mixed fluid, as discussed by De-Silva & Fernando (1998). In the intrusion IJK of figure 16, higher density fluid flows down from the upper part IJ, while the lower density fluid moves up in the lower part KJ to create the entire structure IJK which intrudes into the ambient fluid and moves away from the shear layer. The outflow of the mixed fluid from the shear layer is balanced by external fluid entering the shear layer in thin zones with significant v. The density variation along line BB in figure 16 is

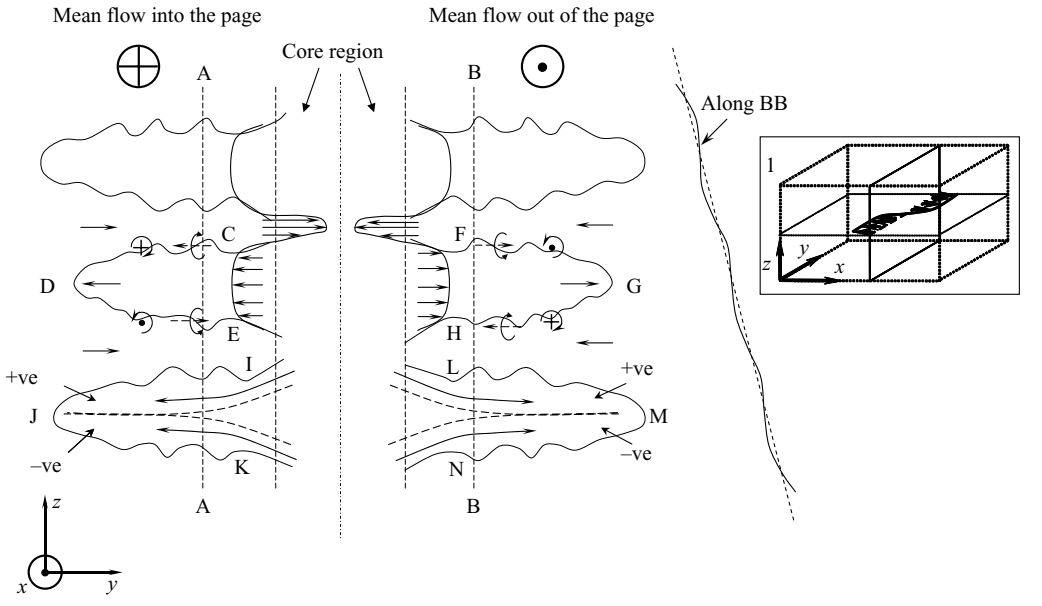

FIGURE 16. Schematic of the intrusion process at the central x-plane.

shown at the right of the schematic. The presence of positive ρ' over negative ρ' at the intrusions decreases the density gradient locally while, in order to maintain the overall imposed density gradient, the density gradient in the inter-intrusion zones increases. Although the density gradient decreases at the intrusions, the total density profile remains statically stable precluding the generation of Rayleigh–Taylor instabilities.

The intrusions are relatively clear at late time. Some of the tips of the intrusions, containing heavier (than ambient) fluid over lighter fluid, have been marked as points A, B and C in figure 17. Generally, the positive-ρ' tongues are observed to have a downward inclination while the corresponding negative-ρ' fluid has an upward inclination, in accord with the schematic, figure 16. The spread of the intrusions in the cross-stream direction is shown by tracking the nose of an intrusion marked by AA_1 in the panels of figure 17. (Due to the periodic boundary condition, the positive-ρ' zone at A_1 has its counterpart of negative ρ' near the top of the flow domain at A.) At time $t = 65.95$, the nose of the intrusion is near $y = 16$; however at $t = 78.27$, it is at $y = 13$. The tips, B and C, exhibit similar outward movement. Unfortunately, the presence of internal gravity waves and the mean shear flow does not allow an accurate quantitative estimate of the velocity of individual intrusion heads. Furthermore, the intrusions are three-dimensional and spatially intermittent.

Secondary vorticity is generated at the intrusions. Figure 18 gives a composite view of the density and vorticity components at late time. The primary vorticity, figure 18(b), is more compact than the density intrusion, figure 18(a), and also than the secondary vorticity fields in figure 18(c, d). It is useful to revisit the sketch of figure 16 to understand how secondary vorticity is generated at the intrusions. At the tip of the intrusion CDE, the cross-stream velocity, v, is negative, while v is positive in the reverse flow zones above and below, resulting in negative ω_x in CD and positive ω_x in DE. Since the intrusions are embedded in a shear layer, ω_y is also created. Inside CDE, the outward flow has smaller streamwise speed than the reverse flow near surface CD which comes from the free stream, and the change δU, over a vertical

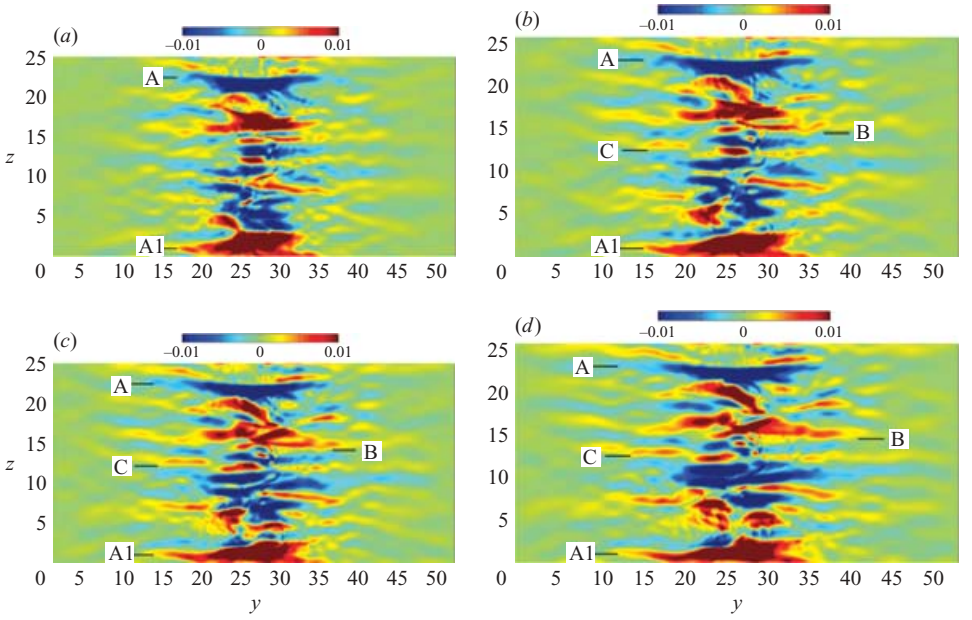

FIGURE 17. ρ' at the centre x-plane at late time for case A5. (*a*) $t = 65.95$, (*b*) $t = 70.23$, (*c*) $t = 74.27$, (*d*) $t = 78.27$.

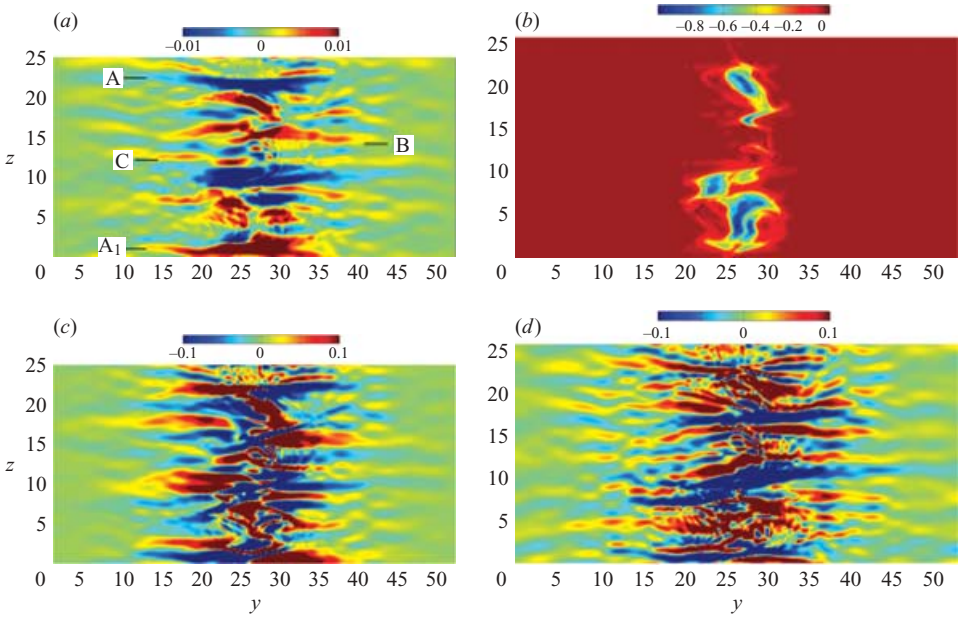

FIGURE 18. Centre x-plane at late time, $t = 79.62$ for case A5. (*a*) ρ', (*b*) ω_z, (*c*) ω_y, (*d*) ω_x.

distance δz, creates cross-stream vorticity, ω_y. As noted on figure 16, at the left side of the shear layer negative ω_x and ω_y are expected at zones of positive ρ', while positive ω_x and ω_y are expected at zones of negative ρ'. However, on the right side of this figure, positive ω_x and ω_y are associated with positive ρ', while negative ω_x and

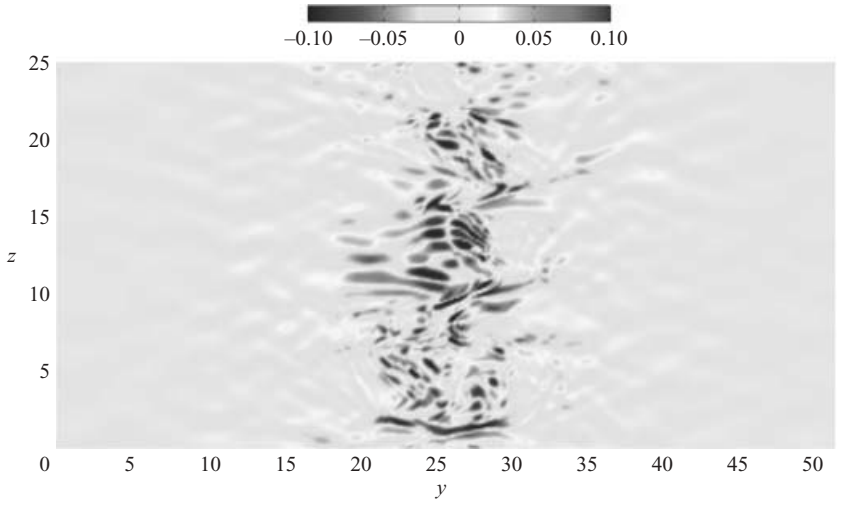

FIGURE 19. $\mathrm{d}w/\mathrm{d}z$ at late times at the central x-plane for case A5, $t = 79.8$.

ω_y are associated with negative ρ'. The agreement of the ρ' and the ω_y field in figure 18(a–c) with that expected from the schematic is particularly good.

Although the ω_x field also shows broad agreement with the expected behaviour, it contains many smaller-scale features, especially at the tip of the intrusions. These additional features are caused by the baroclinic torque (the $-(1/\rho_0)\nabla\rho \times g\boldsymbol{k}$ term in the vorticity equation) associated with the generation and passage of the vortical internal gravity waves. Although internal gravity waves can contribute to ω_y as well, small-scale features are found to be more prominent in a constant-x cut of the ω_x field.

The internal gravity wave field at a late time for case A5 is briefly discussed below. The vertical strain, $\mathrm{d}w/\mathrm{d}z$, is the negative of the horizontal divergence of an incompressible flow field and is often used as a signature of emissions of internal gravity waves (Riley & Lelong 2000; Diamessis *et al.* 2005). The $\mathrm{d}w/\mathrm{d}z$ field is shown at the central x plane at a late time for case A5 in figure 19. The vertical strain in the central zone of the shear layer is associated with turbulence, while that away from the shear layer is associated with the internal gravity waves. In the flow considered here, the internal wave field is found to have smaller ρ' compared to that in the intrusions. The $\mathrm{d}w/\mathrm{d}z$ structures are predominantly inclined to the horizontal, similar to the experimental observations of Dohan & Sutherland (2003) and Flynn & Sutherland (2004), and the simulations of Gourlay *et al.* (2001) and Diamessis *et al.* (2005). These structures also have significant cross-stream extent compared to the shear layer, leading to transfer of momentum and horizontal vorticity away from the shear layer.

6. Structure of dissipation and scalar mixing

There are zones of intense turbulent dissipation, ϵ, that largely coincide with the locations of strong horizontal vorticity. In case A2, ϵ is strong in the braid region between the ω_z rollers, as well as in some locations embedded within the rollers and at their periphery. Strong dissipation is also observed in the dislocations of vortex cores. Regions with large ϵ are sparser in case A5 and, contrary to case A2, are

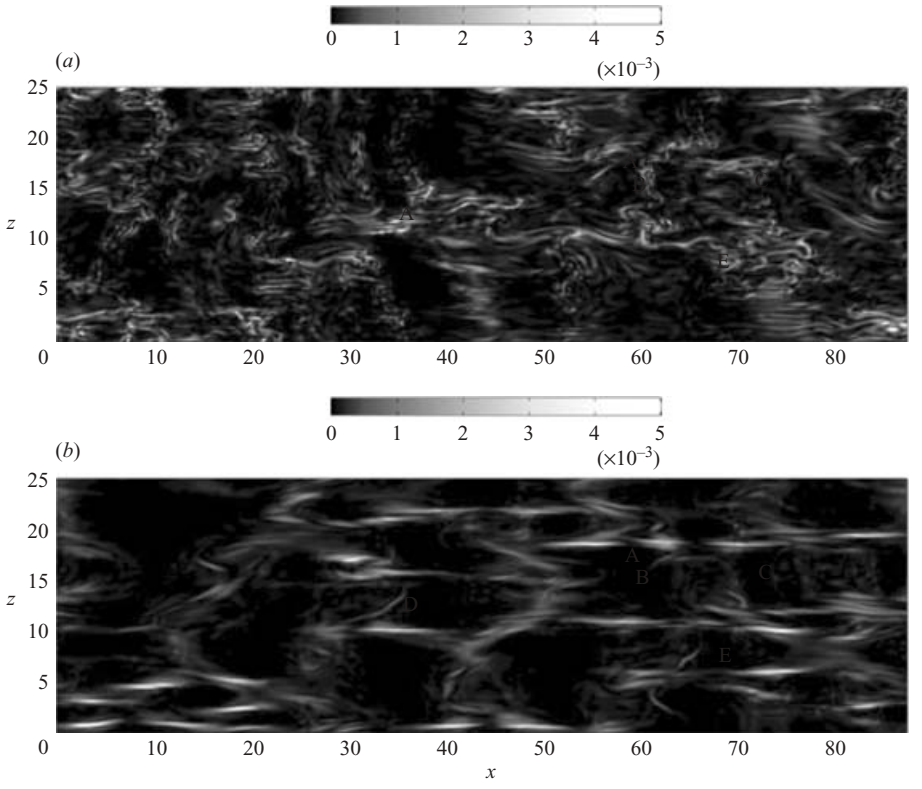

FIGURE 20. Location of turbulent dissipation, ϵ at late times at the central y-plane, (*a*) case A2, $t = 82$ (*b*) case A5, $t = 79.8$.

mainly confined to the dislocations. Thus, the dislocations induced by buoyancy in the vortex cores provides a mechanism for dissipation at high N.

Locations of intense molecular mixing, measured by the dissipation of turbulent potential energy, ϵ_ρ, are quite similar to those of large ϵ as seen by comparing figure 21 with figure 20. Here, ϵ_ρ is defined as

$$\epsilon_\rho = \frac{\nu}{Pr}\frac{g}{\rho_0|\mathrm{d}\overline{\rho}/\mathrm{d}z|}\overline{\frac{\partial\rho'}{\partial x_k}\frac{\partial\rho'}{\partial x_k}} = \frac{1}{2}\frac{g}{\rho_0|\mathrm{d}\overline{\rho}/\mathrm{d}z|}\chi \tag{6.1}$$

where

$$\chi = 2\frac{\nu}{Pr}\overline{\frac{\partial\rho'}{\partial x_k}\frac{\partial\rho'}{\partial x_k}}$$

denotes the dissipation of the density variance. ϵ_ρ signifies irreversible loss of turbulent potential energy to the background density field and can be used as a measure of molecular mixing of the density field (Winters *et al.* (1995), Jacobitz & Sarkar (1998), Riley & deBruynKops (2003)). It was seen in § 5 that ρ' with significant spatial segregation is mainly associated with the ω_z cores. Besides, the ρ' structures also aid in the collapse of sections of the cores to form dislocations. Therefore there is significant $\partial\rho'/\partial x_k$ and associated ϵ_ρ in the vortex cores and the dislocation regions. Similarly the ω_h present at the periphery of the cores and in the braid regions also generates ρ' by rotational motion and the associated $\partial\rho'/\partial x_k$ also contributes to ϵ_ρ. Thus, the locations of ϵ and ϵ_ρ are quite similar.

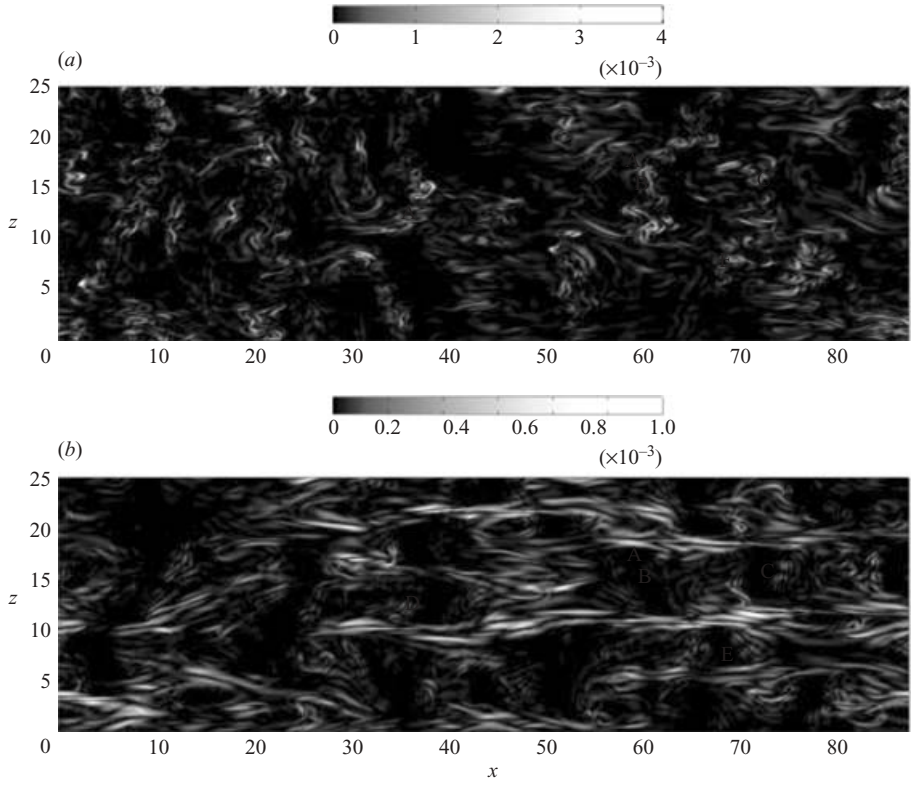

FIGURE 21. Location of dissipation of turbulent potential energy ϵ_ρ at late times at the central y-plane, (a) case A2, $t = 82$ (b) case A5, $t = 79.8$.

The evolution of net dissipation, integrated across the shear layer, is also of interest and its value normalized with ΔU^3 is plotted in figure 22(a). As a reference point, the normalized integrated dissipation for the unstratified case reaches a value of approximately 5.5×10^{-3}. In case A2, integrated ϵ decreases and then becomes relatively constant. The decrease is caused by the reduction of ω_h in the braid and within the rollers due to stratification. However, at later times, new sites of ω_h emerge at the dislocation zones between the rollers, compensating for the reduced ϵ in other zones to keep integrated ϵ relatively constant. In case A5, braid ω_h is damped quite early in the flow and, consequently, integrated ϵ also goes down quickly. However, the annihilation of ω_h helps the core dynamics to become important early in the flow evolution, leading to the development of a lattice with dislocations having intense ω_h and ϵ. This more than compensates for the reduction in ϵ due to the vanishing of braid vortices and explains the late time increase of integrated ϵ for case A5. Similar to the integrated ϵ, the integrated ϵ_ρ in figure 22(b) also remains fairly constant at the later times for case A2, while it increases appreciably for case A5. The continuous formation of small-scale layers of ρ' within the cores and the dislocation regions, and the corresponding $\partial\rho'/\partial x_k$, is responsible for this increase. The high values of both integrated ϵ and ϵ_ρ for case A5 and their increasing trend at late time, in spite of the corresponding high Ri_b of nearly 45, is noteworthy.

The ratio of $\int \epsilon_\rho \, \mathrm{d}y$ and $(\int \epsilon \, \mathrm{d}y + \int \epsilon_\rho \, \mathrm{d}y)$ denotes the ratio of overall irreversible dissipation of potential energy to the overall dissipation of both kinetic and potential energy, and can be used as a measure of diapycnal mixing efficiency at the molecular

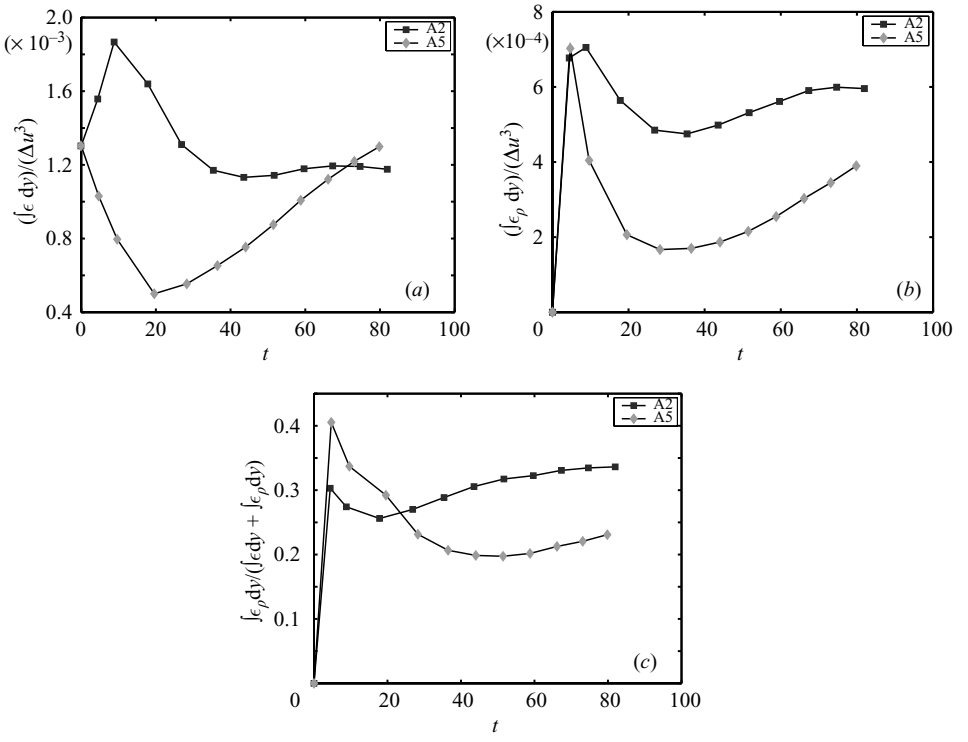

FIGURE 22. Comparison of (*a*) $\int \epsilon \, \mathrm{d}y$, (*b*) $\int \epsilon_\rho \, \mathrm{d}y$ and (*c*) $\int \epsilon_\rho \, \mathrm{d}y / (\int \epsilon \, \mathrm{d}y + \int \epsilon_\rho \, \mathrm{d}y)$ between cases A2 and A5.

level. This ratio, plotted for cases A2 and A5 in figure 22(*c*), is observed to increase for both cases at late times reaching around 0.34 for case A2 and around 0.23 for case A5. This shows that horizontal shear is capable of mixing the density field quite efficiently although there is little overturning motion. $\int \epsilon_\rho \, \mathrm{d}y / \int \epsilon / \mathrm{d}y = \Gamma_d$ (Riley & deBruynKops 2003), not plotted here, also increases with Ri_b and reaches about 0.51 for case A2 and about 0.3 for case A5 at late times. These are of similar order to the late-time values of Γ_d lying between 0.4 and 0.5 observed in the high-Re simulations of Riley & deBruynKops (2003). In their simulations, Γ_d tends to remain quite steady with a slight decaying tendency at late times. However, in our simulations Γ_d is found to increase slightly at late times which is even more pronounced for case A5.

Oceanographers often infer the turbulent eddy diffusivity, K_ρ, from microstructure measurements. If the buoyancy flux, $-B$, is a fixed proportion, Γ, of the turbulent dissipation rate, ϵ, then the eddy diffusivity can be estimated using $K_\rho = \Gamma \epsilon / N^2$, Osborn (1980). The quantity $\Gamma_d = \epsilon_\rho / \epsilon$ can be measured directly in the ocean from temperature gradient and velocity shear data, and is used as a surrogate for the mixing efficiency, Oakey (1985). Studies of the mixing efficiency show that Γ and Γ_d depend on other parameters such as the gradient Richardson number, Reynolds number, shear number, and Prandtl number. The dependence on the Richardson number is especially strong. In many data sets where vertical shear is the source of turbulence, the maximum value of the mixing efficiency is about 0.2. The value of 0.2 is often used to infer K_ρ from ϵ in oceanography. In the present flow, turbulence forced by mean horizontal shear, the values of Γ_d given in the previous paragraph are systematically higher than 0.2.

7. Conclusions

DNS is used to investigate the structural organization of the vorticity, density and dissipation fields in a horizontal-shear layer that evolves in a linearly stratified medium. Cases with several values of N are simulated, all starting with the the same initial mean flow profile and the same initial field of broadband, finite-amplitude velocity perturbations. The effects of stratification on the structural organization of the flow are discussed in detail for cases A2 and A5 which have a moderate and a high initial value of bulk Richardson number Ri_b, respectively, with comparisons drawn with the corresponding unstratified flow when appropriate. In all the stratified cases, Ri_b increases with time so that eventually stratification dominates the dynamics but to a different degree.

The organization of the vorticity field in the stratified cases is found to be remarkably different from the unstratified situation. Although local lumping of the vorticity field is observed in the unstratified case, distinct KH rollers, as observed in transitional shear layers are not discerned, as they are obscured by small-scale vorticity filaments that are distributed chaotically. This is consistent with previous studies of the unstratified shear layer at a relatively high Re beyond mixing transition, Bell & Mehta (1990) and Rogers & Moser (1994). However, in the presence of stratification, coherent columnar vortex cores emerge from the random sea of turbulence. The KH rollers that emerge in the stratified shear layer exhibit pairing, tearing and amalgamation, similar to previous observations in high-Re shear layers exhibiting coherent structures, Hernan & Jimenez (1982) and Dimotakis & Brown (1976).

The formation of organized KH rollers in the stratified shear layer in spite of the high Re at late time and disorganization in the initial conditions is an important result of this work. This effect is linked to the inhibition of vertical transport of fluid by stratification which effectively suppresses the overturning of horizontal vorticity. The suppression of the secondary vorticity causes a 'reverse mixing transition' wherein the natural two-dimensional inviscid instability of the free shear layer becomes increasing important resulting in the emergence of core/braid structures. Organized vortex cores appear when $16 < Nt^* < 20$ in cases A2–A5, with corresponding values of $1.25 < Ri_b < 2.25$. Organized braids also appear but they progressively weaken with time owing to stratification. At the time of emergence, the vortex cores are thicker in case A2 since the dimensional time, t^*, is larger. The organized structures at a given Nt^* are generally more distinct in case A5 compared to the other cases because three-dimensional fluctuations typical of 'unstratified' turbulence are unable to develop since the initial $Ri_b = 1$ is already large. However, later in time, buoyancy induces vertical variability.

The demonstration of how the organized density and vorticity fields couple to bring about significant vertical structure is another important result of this work, and is summarized below. The velocity fluctuations stir up the initial linearly varying density field to create density fluctuations. Short vortex cores with heavier under lighter fluid, stable because of a combination of centrifugal and hydrostatic balance, are observed. However, when there is a horizontal density gradient in a section of a vortex core, it tends to tilt the section through a baroclinic torque. The tilting brings local regions of adjacent vortex cores closer, which are then able to pair locally. The inclined elements collapse to create an organized vorticity network. In case A5, a lattice of organized vorticity (figure 9) consisting of dislocated cores of ω_z and sheets of ω_h at the dislocations emerges which is quite distinct from the hexagonal lattice observed in the unstratified low-Re studies of Comte *et al.* (1992) and Nygaard & Glezer (1994). The collapsed vortical and density structures observed in the present

flow provide another example of the phenomenon of layering in flows with high horizontal Froude number, Fr_h, that has been found in grid turbulence, wakes and oceanic flows as discussed in the introduction. The continuous formation of KH rollers in the present flow provides vortex cores which, being always susceptible to linear and nonlinear (Re increases with time) instabilities associated with stratification and vortex interactions, develop vertical variability. The height of the vortex cores is approximately $6\Delta U/N$ in the DNS. It is noteworthy that buoyancy constrains the vortex core height to be approximately constant, although these cores interact and continually thicken by pairing. Similar to the zig-zag instability, stratification imposes a distinct vertical scale on the coherent vortices in this flow although the present problem of a turbulent flow with many interacting, co-rotating vortices is different from the isolated counter-rotating vortex pair studied by Billant & Chomaz (2000*a*). The radius of the vortex cores increases with time due to pairing so that the initial tall columns of vorticity tend towards a pancake shape. Terms in the vorticity transport equation are examined. The baroclinic torque is found to be large in the inclined vortex cores, showing the important coupling of buoyancy to vorticity. Although horizontal advection is generally dominant, vertical stretching/compression is also important to the evolution of ω_z at localized sites. Viscous diffusion of all components of vorticity is found to be strong at the dislocation sites whose thickness in the DNS is approximately $15\sqrt{\nu/N}$.

There are locations of strong dissipation, ϵ, in the flow which, for the most part, coincide with those of large horizontal vorticity, ω_h. In case A2, ω_h and ϵ are found in the braid region, within the cores and in the zones of dislocations, with ω_h and ϵ decreasing in the braid region and increasing in the dislocations at late times. In case A5, ϵ is noted within the cores and mainly in the dislocation zones, with the values at the dislocations intensifying at late times. Regions of strong molecular mixing of the density field, ϵ_ρ, are largely concurrent with large ϵ. Both the overall dissipation and density mixing remain significant at high Ri_b although the responsible structures are qualitatively different from the unstratified case. The capacity of the high-Ri_b horizontal-shear layer to dissipate and mix vertically in spite of the strong stabilizing effect of stratification is noteworthy.

A stratified shear layer with vertical mean shear is a related flow that has been the subject of much study. Such a shear layer eventually collapses; $Ri_b \to 0.3$–0.5 depending on the details of the experiment. In the present case with mean horizontal shear, the shear layer continues to grow since the formation of KH rollers and their pairing correspond to horizontal flow, not directly affected by buoyancy. The maximum value of the mixing efficiency is observed to be larger here relative to the value of 0.2, based on vertical shear flow data, that is often used by oceanographers. When $Ri_b > 0.5$ in flows with vertical mean shear, the mixing efficiency becomes small while, in the present flow, the mixing efficiency does not show such a large decrease even at $Ri_b \simeq 40$. Thus, the cumulative vertical mixing induced by horizontal shear may be significant in environmental flows even when the magnitude of horizontal shear is small. The organized lattice of vorticity found here at high Nt^* has not been observed in previous studies of a stratified shear layer with vertical shear.

The dynamics at the edges of the shear layer have also been investigated. Patches of light and heavy fluid converge owing to buoyancy and the combined fluid patches spread out as intrusions, moving outward from the shear layer. These intrusions have significant streamwise, vertical and temporal variability, and are sites for generation of secondary vorticity. Opposition to overturning by baroclinic forces in the stratified flow leads to the emission of internal gravity waves which propagate

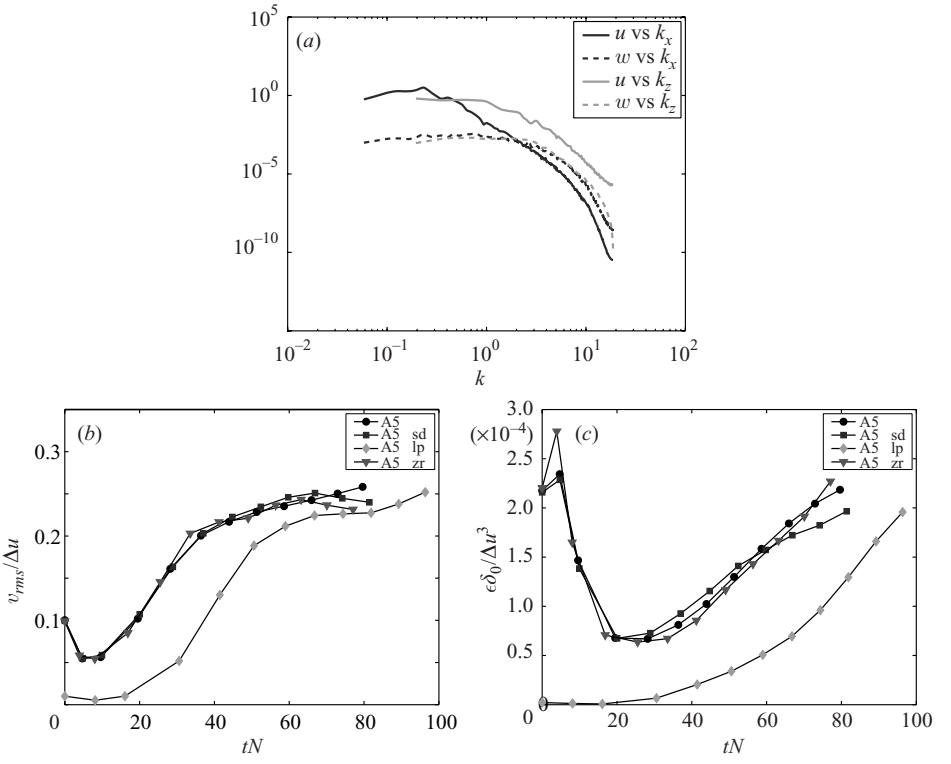

FIGURE 23. (*a*) Vertical and horizontal spectra of u and w at late time, $t = 79.8$ for case A5. (*b*) Comparison of the evolution of centreline v_{rms} for the different high-stratification simulations. A5 is the original high stratification case described in table 1. The other cases are described in table 2. (*c*) Evolution of the centreline ϵ for the different high stratification cases.

away from the shear layer. The internal waves are visualized using the vertical strain $\mathrm{d}w/\mathrm{d}z$.

Thus, a high-Re and high-Ri_b shear layer with horizontal shear exhibits remarkably rich dynamics: turbulence, coherent structures including dislocated vortex columns and collapsed sheets of vorticity, density-driven intrusions, and internal gravity waves. There is significant diapycnal mixing and dissipation which would be missed by two-dimensional or hydrostatic simulations. This work reports the structural organization of the vorticity, density and dissipation fields that is brought about by buoyancy effects. Also of importance is the statistical evolution, including Reynolds stresses, spectra, correlations, length scales, eddy diffusivity, and energy balances which will be reported in a later paper.

The support of NSF OCE-9818912 and OCE-0411938 is gratefully acknowledged. Computational time was provided through an NPACI allocation.

Appendix

Dislocations of the vertical vorticity, ω_z, occurs over small vertical scales, especially in case A5 with high N. To ensure that the small scales are resolved in these simulations, the centreline u and w velocity spectra in the x- and z-directions are plotted in figure 23(*a*). A decay of energy at high wavenumbers is noted without

Case	$[L_x \times L_y \times L_z]/\delta_{\omega,0}$	$N_x \times N_y \times N_z$	$q^2/\Delta u^2$	Phase (compared to A5)
A5sd	$107.5 \times 64.5 \times 32.25$	$640 \times 384 \times 192$	0.029	different
A5lp	$107.5 \times 64.5 \times 32.25$	$640 \times 384 \times 192$	0.00029	same
A5zr	$64.5 \times 32.25 \times 21.5$	$384 \times 192 \times 256$	0.029	same

TABLE 2. Description of the different cases simulated by changing parameters of case A5 to check the effects of initial condition and grid resolution.

any energy accumulation, with $E_u(k_x)$ and $E_u(k_z)$ decaying by 10 and 5 decades, respectively. The vertical velocity, w, has relatively smaller energy in the larger scales. A decay of about 5 decades is observed in both $E_w(k_x)$ and $E_w(k_z)$.

Figures 23(b) and 23(c) show the evolution of centreline v_{rms} and ϵ for the original high-stratification case A5 and different variants, based on initial conditions and grid resolution, as described in table 2. To further ensure adequacy of z resolution, case A5zr has been simulated in a smaller domain, with half the z grid spacing of case A5. The agreement of centreline v_{rms} as well as ϵ between cases A5 and A5zr confirms the adequacy of the z resolution of the reported simulations.

The effect of changing initial conditions is studied through two new simulations. Case A5sd has the same perturbation energy as case A5; however the phase of the perturbation velocity fields is different. Case A5lp has 1/100 of the perturbation energy of case A5, but the perturbation field has the same phase. The behaviour of case A5sd in figure 23(b, c) is very similar to case A5, signifying the unimportance of the phase of the perturbations to the statistical evolution of the flow, although the location of vortex cores in visualizations (not shown) is quite different.

The initial evolution of case A5lp is quite different from case A5. The low initial level of perturbations allows the development of smooth organized structures with significantly less small-scale vertical variability than the distinct lattice structure for case A5 at similar time. Correspondingly, the early values of v_{rms} and ϵ are also smaller for case A5lp in Figure 23(b, c). However, the late-time dynamics is dominated by the dislocated lattice of ω_z similar to that observed in case A5, and hence the statistics are also similar. To summarize, the organized vorticity and density fields at large Nt^* found here do not have significant dependence on the initial fluctuations.

REFERENCES

ARMENIO, V. & SARKAR, S. 2002 An investigation of stably stratified turbulent channel flow using large-eddy simulation. *J. Fluid Mech.* **459**, 1–42.

ARMENIO, V. & SARKAR, S. 2004 Mixing in a stably-stratified medium by horizontal shear near vertical walls. *Theor. Comput. Fluid Dyn.* **17**, 331–349.

BARRY, M. E., IVEY, G. N., WINTERS, K. B. & IMBERGER, J. 2001 Measurements of diapycnal diffusivities in stratified fluids. *J. Fluid Mech.* **442**, 267–291.

BECKERS, M., VERZICCO, R., CLERCX, H. J. H. & VAN HEIJST, G. J. F. 2001 Dynamics of pancake-like vortices in a stratified fluid: experiments, model and numerical simulations. *J. Fluid Mech.* **433**, 1–27.

BELL, J. H. & MEHTA, R. D. 1990 Development of a two-stream mixing layer from tripped and untripped boundary layers. *AIAA J.* **28**, 2034–2042.

BERNAL, L. P. & ROSHKO, A. 1986 Streamwise vortex structure in plane mixing layers. *J. Fluid Mech.* **170**, 499–525.

BILLANT, P. & CHOMAZ, J.-M. 2000*a* Experimental evidence for a new instability of a vertical columnar vortex pair in a strongly stratified fluid. *J. Fluid Mech.* **418**, 167–188.

Billant, P. & Chomaz, J.-M. 2000*b* Three-dimensional stability of a vertical columnar vortex pair in a stratified fluid. *J. Fluid Mech.* **419**, 65–91.

Bonneton, P., Chomaz, J. M. & Hopfinger, E. J. 1993 Internal waves produced by the turbulent wake of a sphere moving horizontally in a stratified fluid. *J. Fluid Mech.* **254**, 23–40.

Bonnier, M., Bonneton, P. & Eiff, O. 1998 Far-wake of a sphere in a stably stratified fluid: characterization of the vortex structures. *Appl. Sci. Res.* **59**, 269–281.

Browand, F. K., Guyomar, D. & Yoon, S. C. 1987 The behavior of a turbulent front in a stratified fluid: experiments with an oscillating grid. *J. Geophys. Res.* **92**, 5329–5341.

Browand, F. K. & Troutt, T. R. 1980 A note on spanwise structure in the two-dimensional mixing layer. *J. Fluid Mech.* **97**, 771–781.

Brown, G. L. & Roshko, A. 1974 Density effects and large structure in turbulent mixing layers. *J. Fluid Mech.* **64**, 775–816.

Caldwell, D. R., Brubaker, J. B. & Neal, V. T. 1978 Thermal microstructure on a lake slope. *Limnol. Oceanogr.* **23**, 372–374.

Caulfield, C. P. & Peltier, W. R. 2000 The anatomy of the mixing transition in homogeneous and stratified free shear layers. *J. Fluid Mech.* **413**, 1–47.

Chandrsuda, C., Mehta, R. D., Weir, A. D. & Bradshaw, P. 1978 Effect of free-stream turbulence on large structure in turbulent mixing layers. *J. Fluid Mech.* **85**, 693–704.

Collis, S. S., Lele, S. K., Moser, R. D. & Rogers, M. M. 1994 The evolution of a plane mixing layer with spanwise nonuniform forcing. *Phys. Fluids* **6**, 381–396.

Comte, P., Lesieur, M. & Lamballais, E. 1992 Large-scale and small-scale stirring of vorticity and a passive scalar in a 3-D temporal mixing layer. *Phys. Fluids* **4**, 2761–2778.

Corcos, G. M. & Lin, S. J. 1984 The mixing layer: deterministic models of a turbulent flow. Part 2. The origin of the three-dimensional motion. *J. Fluid Mech.* **139**, 67–95.

De-Silva, I. P. D. & Fernando, H. J. S. 1998 Experiments on collapsing turbulent regions in stratified fluids. *J. Fluid Mech.* **358**, 29–60.

Diamessis, P. J., Domaradzki, J. A. & Hesthaven, J. S. 2005 A spectral multidomain penalty method model for the simulation of high Reynolds number localized incompressible stratified turbulence. *J. Comput. Phys.* **202**, 298–322.

Dimotakis, P. E. & Brown, G. L. 1976 Mixing layer at high Reynolds-number – large-structure dynamics and entrainment. *J. Fluid Mech.* **78**, 535–560.

Dohan, K. & Sutherland, B. 2003 Internal wave generated from a turbulent mixed region. *Phys. Fluids* **15**, 488–498.

Dommermuth, D. G., Rottman, J. W., Innis, G. E. & Novikov, E. A. 2002 Numerical simulation of the wake of a towed sphere in a weakly stratified fluid. *J. Fluid Mech.* **473**, 83–101.

E, X. & Hopfinger, E. 1986 On mixing across an interface in stably-stratified fluid. *J. Fluid Mech.* **166**, 227–244.

Farmer, D., D'Asaro, E., Trevorrow, M. & Dairiki, G. 1995 Three-dimensional structure in a tidal convergence front. *Continental Shelf Res.* **15**, 1649–1673.

Fernando, H. J. S. 2003 Turbulent patches in a stratified shear flow. *Phys. Fluids* **15**, 3164–3169.

Fincham, M., Maxworthy, T. & Spedding, G. R. 1996 Energy dissipation and vortex structure in freely-decaying, stratified grid turbulence. *Dyn. Atmos. Oceans* **23**, 155.

Flament, P., Lumpkin, R., Tournadre, J. & Armi, L. 2001 Vortex pairing in an unstable anticyclonic shear flow: discrete subharmonics of one pendulum day. *J. Fluid Mech.* **440**, 401–409.

Flynn, M. R. & Sutherland, B. R. 2004 Intrusive gravity currents and internal gravity wave generation in stratified fluid. *J. Fluid Mech.* **514**, 355–383.

Garg, R. P., Ferziger, J. H., Monismith, S. G. & Koseff, J. R. 2000 Stably stratified turbulent channel flows. I. Stratification regimes and turbulence suppression mechanism. *Phys. Fluids* **12**, 2569.

Gibson, C. H. 1980 Fossil temperature, salinity, and vorticity turbulence in the ocean. In *Marine Turbulence* (ed. J. Nihoul), pp. 221–257. Elsevier.

Godoy-Diana, R. & Chomaz, J.-M. 2003 Effect of the Schmidt number on the diffusion of axisymmetric pancake vortices in a stratified fluid. *Phys. Fluids* **15**, 1058–1064.

Gourlay, M. J., Arendt, S. C., Fritts, D. C. & Werne, J. 2001 Numerical modeling of initially turbulent wakes with net momentum. *Phys. Fluids* **13**, 3783–3802.

Hernan, M. A. & Jimenez, J. 1982 Computer-analysis of a high-speed film of the plane turbulent mixing layer. *J. Fluid Mech.* **119**, 323.

Herring, J. R. & Metais, O. 1989 Numerical experiments in forced stably stratified turbulence. *J. Fluid Mech.* **202**, 97–115.

Hussain, A. K. M. F. 1983 Coherent structures – reality and myth. *Phys. Fluids* **26**, 2816–2850.

Ivey, G. N. & Corcos, G. M. 1982 Boundary mixing in a stratified fluid. *J. Fluid Mech.* **121**, 1–26.

Jacobitz, F. G. & Sarkar, S. 1998 The effect of nonvertical shear on turbulence in a stably stratified medium. *Phys. Fluids* **10**, 1158–1168.

Jacobitz, F. G. & Sarkar, S. 1999 A direct numerical study of transport and anisotropy in a stably stratified turbulent flow with uniform horizontal shear. *Flow, Turbulence Combust.* **63**, 343–360.

Johannessen, J., Schuman, R., Digranes, G., Lyzenga, D., Wackerman, C., Johannessen, O. & Vachon, P. W. 1996 Coastal ocean fronts and eddies imaged with ERS 1 synthetic aperture radar. *J. Geophys. Res.* **101**, 6651–6667.

Kimura, Y. & Herring, J. R. 1996 Diffusion in stably stratified turbulence. *J. Fluid Mech.* **328**, 253–269.

Klaassen, G. P. & Peltier, W. R. 1991 The influence of stratification on secondary instability in free shear layers. *J. Fluid Mech.* **227**, 71–106.

Komori, S., Ueda, H., Ogino, F. & Mizushina, T. 1983 Turbulence structures in stably stratified open-channel flow. *J. Fluid Mech.* **130**, 13–26.

Koop, C. & Browand, F. 1979 Instability and turbulence in a stratified fluid with shear. *J. Fluid Mech.* **93**, 135–159.

Lasheras, J. C., Cho, J. S. & Maxworthy, T. 1986 On the origin and evolution of streamwise vortical structures in a plane, free shear layer. *J. Fluid Mech.* **172**, 231–258.

Lasheras, J. C. & Choi, H. 1988 Three-dimensional instability of a plane free shear-layer: an experimental study of the formation and evolution of streamwise vortices. *J. Fluid Mech.* **189**, 53–86.

Lee, V. & Caulfield, C. P. 2001 Nonlinear evolution of a layered stratified shear flow. *Dyn. Atmos. Oceans* **34**, 103–124.

Lilly, D. K. 1983 Stratified turbulence and the mesoscale variability of the atmosphere. *J. Atmos. Sci.* **40**, 749.

Lin, J. T. & Pao, Y. H. 1979 Wakes in stratified fluids. *Annu. Rev. Fluid Mech.* **11**, 317–338.

Lin, Q., Lindberg, W., Boyer, D. & Fernando, H. 1992 Stratified flow past a sphere. *J. Fluid Mech.* **240**, 315–354.

Linden, P. 1975 Deepening of a mixed layer in a stratified fluid. *J. Fluid Mech.* **71**, 385–405.

Liu, Y. N., Maxworthy, T. & Spedding, G. R. 1987 Collapse of a turbulent front in a stratified fluid 1. Nominally two-dimensional evolution in a narrow tank. *J. Geophys. Res.* **92**, 5427–5433.

Majda, A. J. & Grote, M. J. 1997 Model dynamics and vertical collapse in decaying strongly stratified flows. *Phys. Fluids* **9**, 2932–2940.

Metais, O. & Herring, J. R. 1989 Numerical simulations of freely evolving turbulence in stably stratified fluids. *J. Fluid Mech.* **202**, 117–148.

Metcalfe, R. W., Orszag, S. A., Brachet, M. E., Menon, S. & Riley, J. J. 1987 Secondary instability of a temporally growing mixing layer. *J. Fluid Mech.* **184**, 207–243.

Moser, R. D. & Rogers, M. M. 1993 The three-dimensional evolution of a plane mixing layer - pairing and transition to turbulence. *J. Fluid Mech.* **247**, 275–320.

Müller, P., Holloway, G., Henyey, F. & Pomphrey, N. 1986 Nonlinear interactions among gravity waves. *Rev. Geophys.* **24**, 493–536.

Munk, W., Armi, L., Fischer, K. & Zachariasen, F. 2000 Spirals on the sea. *Proc. R. Soc. Lond.* A **456**, 1217–1280.

Nygaard, K. J. & Glezer, A. 1991 Evolution of streamwise vortices and generation of small-scale motion in a plane mixing layer. *J. Fluid Mech.* **231**, 257–301.

Nygaard, K. J. & Glezer, A. 1994 The effect of phase variations and cross-shear on vortical structures in a plane mixing layer. *J. Fluid Mech.* **276**, 21–59.

Oakey, N. S. 1985 Statistics of mixing parameters in the upper ocean during JASIN Phase 2. *J. Phys. Oceanogr.* **15**, 1662–1675.

Osborn, T. R. 1980 Estimates of the local rate of vertical diffusion from dissipation measurements. *J. Phys. Oceanogr.* **10**, 83–89.

Pantano, C. & Sarkar, S. 2002 A study of compressibility effects in the high-speed turbulent shear layer using direct simulation. *J. Fluid Mech.* **451**, 329–371.

Pierrehumbert, R. T. & Widnall, S. E. 1982 The two- and three-dimensional instabilities of a spatially periodic shear layer. *J. Fluid Mech.* **114**, 59–82.

Praud, O., Fincham, A. M. & Sommeria, J. 2005 Decaying grid turbulence in a strongly stratified fluid. *J. Fluid Mech.* **522**, 1–33.

Riley, J. J. & deBruynKops, S. M. 2003 Dynamics of turbulence strongly influenced by buoyancy. *Phys. Fluids* **15**, 2047–2059.

Riley, J. J. & Lelong, M.-P. 2000 Fluid motions in the presence of strong stable stratification. *Annu. Rev. Fluid Mech.* **32**, 613–657.

Rogers, M. M. & Moser, R. D. 1994 Direct simulation of a self-similar turbulent mixing layer. *Phys. Fluids* **6**, 903–923.

Smyth, W. & Moum, J. 2000*a* Anisotropy of turbulence in stably stratified mixing layers. *Phys. Fluids* **12**, 1343–1362.

Smyth, W. & Moum, J. 2000*b* Length scales of turbulence in stably stratified mixing layers. *Phys. Fluids* **12**, 1327–1342.

Spedding, G. R. 1997 The evolution of initially turbulent bluff-body wakes at high internal Froude number. *J. Fluid Mech.* **337**, 283–301.

Spedding, G. R. 2002 Vertical structure in stratified wakes with high initial Froude number. *J. Fluid Mech.* **454**, 71–112.

Spedding, G. R., Browand, F. K. & Fincham, A. M. 1996 Turbulence, similarity scaling and vortex geometry in the wake of a towed sphere in a stably stratified fluid. *J. Fluid Mech.* **314**, 53–103.

Staquet, C. 2000 Mixing in a stably stratified shear layer: two- and three-dimensional numerical experiments. *Fluid Dyn. Res.* **27** (6), 367–404.

Strang, E. J. & Fernando, H. J. S. 2001 Entrainment and mixing in stratified shear flows. *J. Fluid Mech.* **428**, 349–386.

Sutherland, B., Caulfield, C. & Peltier, W. R. 1994 Internal gravity-wave generation and hydrodynamic instability. *J. Atmos. Sci.* **51**, 3261–3280.

Sutherland, B. & Linden, P. 1998 Internal wave excitation from stratified flow over a thin barrier. *J. Fluid Mech.* **377**, 223–252.

Thorpe, S. A. 1973 Experiments on instability and turbulence in a stratified shear flow. *J. Fluid Mech.* **61**, 731–751.

Thorpe, S. A. 1982 On the layers produced by rapidly oscillating a vertical grid in a uniformly stratified fluid. *J. Fluid Mech.* **124**, 391–409.

Voropayev, S. I., Smirnov, S. A. & Brandt, A. 2001 Dipolar eddies in a stratified shear flow. *Phys. Fluids* **13**, 3820–3823.

Winant, C. D. & Browand, F. K. 1974 Vortex pairing: the mechanism of turbulent mixing-layer growth at moderate Reynolds number. *J. Fluid Mech.* **63**, 237–255.

Winters, K. B., Lombard, P. N., Riley., J. J. & DAsaro, E. A. 1995 Available potential energy and mixing in density-stratified fluids. *J. Fluid Mech.* **289**, 115–128.